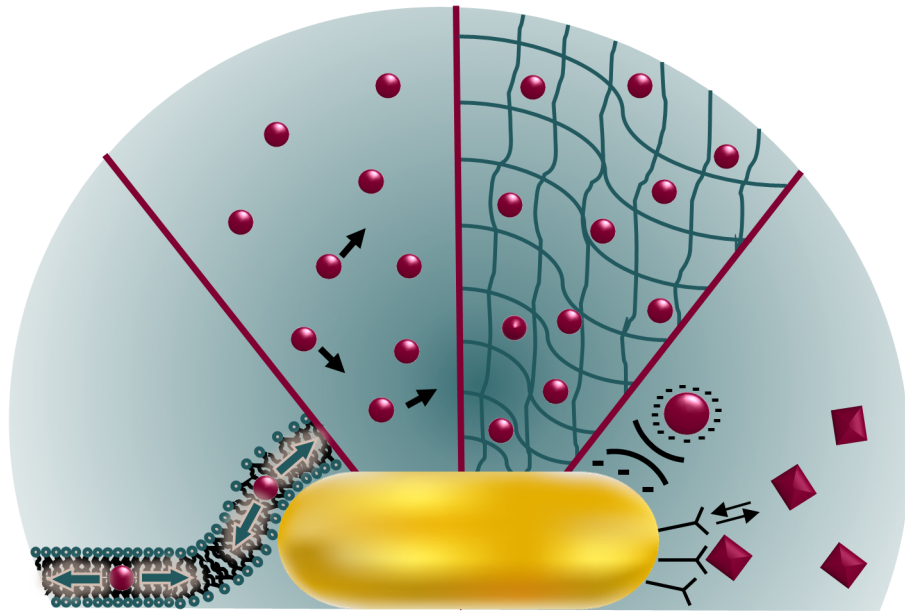


Dark-field Spectroscopy on Single Plasmonic Gold Nanorods -New Methods-



Dissertation zur Erlangung des Grades
“Doktor der Naturwissenschaften” im Promotionsfach Chemie
am Fachbereich Chemie, Pharmazie und Geowissenschaften
der Johannes Gutenberg Universität in Mainz

Verena Wulf

geb. in Heidelberg

Mainz, 2016

Tag der mündlichen Prüfung:

16.06.2016

Der Kampf gegen Gipfel vermag ein Menschenherz auszufüllen. Wir müssen uns Sisyphos als einen glücklichen Menschen vorstellen.

-Albert Camus-

Abstract

Nanomaterials find widespread application particularly as sensors in biochemistry and biophysics taking advantage of their sharp spectral plasmon absorption and scattering peak and its sensitivity to refractive index changes in the near surrounding of the particle. Having a plasmon resonance in the visible wavelength regime gold nanorods are used as refractive index sensors in single particle dark-field micro-spectroscopy, a technique that enables to resolve single particle plasmon shifts below 1 nm, which already permits single protein detection. A variety of possibilities to use dark-field microscopy on plasmonic gold particles is already reported reaching from *in vivo* diagnostics to basic research on plasmons. The improvement of these methods or development of new ones is a large field, reaching from sensor design to setup development.

For this purpose, I introduced silica coated nanoparticles as sensors in dark-field microscopy, which show versatile possibilities, although the accessibility of the sensor surface is decreased by a rigid but porous shell. Taking advantage of their porosity silica coated gold nanorods are able to filter out analytes exceeding a certain threshold in size and let smaller ones enter for detection, a principle highly requested for sensing in multi-component media like blood serum. Further having a rigid shell, whose thickness can be quantified in electron microscopy, these particles can be used to experimentally determine particle specific parameters like the sensing distance on single particle level.

As an improvement of an existing method (our so called NanoSPR), a technique to determine simultaneously the binding constants of an analyte with several receptors, I show that NanoSPR can also be used to identify the adsorbed species. Many proteins build dimers or higher ordered oligomers, whether between each other or with other components, but for some of those the reactive species is not yet identified. With an oligomer forming protein (IM30) as an example it was possible to identify the protomers or lower ordered oligomers of this protein as active binding species and determine their thermodynamic binding affinity from the same experiment.

Tuning a setup to high time resolution spectroscopy allows for measuring diffusion of particles through the sensing volume of a nanorod. I proved the feasibility of this method with the help of a model system of diffusing nanoparticles, whose diffusion times showed from physics expected dependencies. The consistency of this method was also shown by varying the nanoparticle material, size and their surface chemistry. Investigating the free diffusion of particles close to the sensor surface is the first step to investigate interactions between the particle (e.g. a protein) and the surface. If interactions play a role they lower the diffusion time of the system in thermodynamic equilibrium, an effect that can be used to extract binding constants free from unintended influence of mass transport. Measuring also weak interactions between the proteins and a surface covering molecule happening at short timescales is an interesting method in material science when working on anti-biofouling agents.

List of publications

- **Diffusion sensing with plasmonic gold nanorods.**
V. Wulf, F. Knoch, T. Speck, C. Sönnichsen
submitted
- **Organization into higher-ordered ring structures counteracts membrane binding of IM30, a protein associated with inner membranes in chloroplasts and cyanobacteria.**
J. Heidrich, V. Wulf, R. Hennig, M. Saur, J. Markl, C. Sönnichsen, and D. Schneider
Journal of Biological Chemistry **2016**, doi:10.1074/jbc.M116.722686
- **Multiple Internalization Pathways of Polyelectrolyte Multilayer Capsules into Mammalian Cells.**
L. Kastl, D. Sasse, V. Wulf, R. Hartmann, J. Mircheski, C. Ranke, S. Carregal-Romero, J. A. Martinez-Lopez, R. Fernandez-Chacon, W. Parak
ACS Nano **2013**, *7*, 6605-6618.
- **The Challenge To Relate the Physicochemical Properties of Colloidal Nanoparticles to Their Cytotoxicity.**
P. Rivera-Gil, D. Jimenez de Aberasturi, V. Wulf, B. Pelaz, P. Del Pino, Y. Y. Zhao, JM De La Fuente, I Ruiz de Larramendi, T. Rojo, X. J. Liang, W. Parak
Accounts of Chemical Research **2013**, *46*, 743-749.
- **The State of Nanoparticle-Based Nanoscience and Biotechnology: Progress, Promises, and Challenges.**
B. Pelaz, S. Jaber, D. Jimenez de Aberasturi, V. Wulf, T. Aida, J. M. de la Fuente, J. Feldmann, H. Gaub, L. Josephson, C. Kagan, N. Kotov, L. Liz-Marzan, H. Mattoussi, P. Mulvaney, C. Murray, A. Rogach, P. Weiss, I. Willner, W. Parak
ASC Nano **2012**, *6*, 8468-8483
- **Directed deposition of silicon nanowires using neopentasilane as precursor and gold as catalyst.**
B. Kampken, V. Wulf, N. Auner, M. Winhold, M. Huth, D. Rhinow, A. Terfort
Beilstein Journal of Nanotechnology **2013**, *3*, 535-545.

Contents

I Introduction and Theoretical Background	1
Plasmonic Metal Nanoparticles	1
Metal nanoparticles in biomedical applications	1
Theoretical basics of single localized surface plasmon resonance sensing	2
Single Gold Nanorods as Sensors	5
Approximating sensing parameters by BEM calculations	5
Theoretical calculations help for sensor design	7
State of the Art: Refractive Index Sensing with Dark-field Microscopy	11
Multiplexed plasmon sensors	11
NanoSPR sensors to quantify multiple protein-protein binding affinities	12
Diffusion sensing and determination of surface interactions	13
Overview	14
II Sensing with Single Plasmonic Gold Nanorods - New Methods	15
Dark-field Micro-spectroscopy Setups: Measuring Fast Dynamics Requires High Time Resolution	15
Abstract	15
Routine setup and total inter reflection (TIR)-setup	16
Fast measurements are mainly possible because of camera settings	18
Super continuum white-light laser is a suitable light source to achieve high photon density	19
Setup improvements for higher stability and better repeatability	20
Noise dependency on scattering intensity	22
An increased gain influences intensity fluctuations	24
Setup and measurement procedure was improved mechanically, software-wise and concerning the understanding of noise	24

Silica Coated Gold Nanorods as Dark-field Sensors: A Sensor with Molecular Weight Cut-off and a Mean to Investigate Sensing Distance	27
Abstract	27
Silica coated gold nanorods find widespread application in sensing	28
Taking advantage of silica coating in single particle dark-field spectroscopy	28
Silica shells are homogeneous with an ensemble standard deviation of around 10%	29
Pore volume of silica shells can be estimated from sensitivity measurements	30
Blocking of sensing distance for analytes with a certain molecular weight cut-off	32
Silica-coated particles can be used as reference particles for single wavelength measurements	33
Proof-of-principle for silica coated nanorods as sensors in dark-field microscopy	35
NanoSPR for Oligomer-Forming Proteins: Investigating the Adsorbed Species and Its Binding Affinity Simultaneously	37
Abstract	37
Adsorption on small sensors	38
IM30 (Vipp1) – a very important protein in plastids	39
Lipid coated gold-nanorods as sensors have advantages to supported lipid bilayers	40
Lipid coated particles are highly stable and sensitive to IM30	41
The shift-sizes of an IM30 ring-structure can be calculated	42
Adsorption behavior of the protein gives insight in adsorbed species	43
Thermodynamic dissociation constant K_D of IM30 and PG-bilayers was measured	45
NanoSPR can be used to determine the adsorbed species of a protein	46
Gold Nanorods as Plasmonic Sensors for Particle Diffusion and Surface Interactions	47
Abstract	47
A variety of techniques to detect diffusion of particles has a variety of potentials	48
Diffusion sensing with nanorods: A first step to detect surface interactions	48
Setup time resolution is sufficient to measure diffusion of particles	50
Choosing sensor particles: The bigger the better	51
Fluctuation measurements and signal autocorrelation	52
Theoretical model enables sensor calibration	53
Diffusion close to a wall is slowed down due to an increased viscous drag	56
Diffusion coefficients of different types of diffusors show consistency of the method	57
Increasing the ionic strength of the medium, does not influence measurements	58

III	Summary	61
IV	Appendix	63
	Silica-coated gold nanorods as sensors	63
	Materials	63
	Silica coating of gold nanorods	63
	Calcination of the silica shell	63
	NanoSPR for Oligomer-forming Proteins	64
	Materials	64
	Preparation of DOPG-lipids	64
	Preparation of DOPG functionalized particles	64
	NanoSPR experiments	65
	Gold Nanorods as Plasmonic Sensors for Particle Diffusion	66
	Materials	66
	Nanosensor synthesis and characterization	66
	Diffusor synthesis and functionalization	67
	Refractive index measurements of glycerol/water mixtures	67
	Viscosimetric measurements	67
	Determination of the hydrodynamic radius via dynamic light scattering	68
	Explicit expression of Z and H	69
	Background signal is uncorrelated and no medium effects are observable	69
	The scattering intensity of the diffusors themselves does not influence measurements	70
	Calculation of diffusion coefficients from fitting parameters:	71
V	References	73
VI	Acknowledgment	79
VII	Curriculum Vitae	81

List of Figures

1	Plasmonic properties of noble metal nanoparticles.	2
2	Calculating the sensing parameters for gold nanorods.	6
3	Relating sensitivity and sensing distance to particle geometries.	7
4	Dependency of $\Delta\lambda_{res}$ on sensor size.	8
5	Sensing distance and sensor design.	9
6	Multiplexed plasmon sensors.	11
7	Diffusion sensing and surface interactions.	13
8	Scheme of the two different setups.	16
9	Camera settings that enable fluctuation measurements.	18
10	Spectral distribution and stability of the laser intensity.	20
11	Setup stabilization.	21
12	Improving precision of focusing to obtain better repeatability.	22
13	Noise dependency on exposure time.	22
14	Effect of an increased gain on noise.	23
15	Influence of camera gain settings on intensity fluctuations.	24
16	Evaluation of the silica shell homogeneity.	29
17	Sensitivity measurements with silica coated gold nanorods.	31
18	Silica coated gold nanorods as sensors with a molecular weight cut-off are only sensitive to smaller molecules.	32
19	Sensing principle for single wavelength measurements.	33
20	Silica coated gold nanorods as reference particles in single wavelength measurements.	34
21	Difference in protein adsorption behavior on big sensors (SPR) and on nanosensors.	38
22	IM30 is an oligomer-forming protein, that forms ring structures and adsorb on negatively charged lipids.	39
23	Strategies to obtain lipid bilayer covered nanosensors.	40
24	Functionalization is successful and lipid coated particles are sensitive to IM30.	41
25	Quantification of the shift size during adsorption.	44
26	Thermodynamic dissociation constant determined via NanoSPR shows binding affinity for smaller ordered oligomers.	45
27	Scheme of possible applications of diffusion sensing by nanorods.	49

28	Theoretical considerations on possibility of diffusion measurements.	50
29	Measuring particle diffusion as plasmon resonance fluctuations.	52
30	Diffusion times $\tau_{ }$ show the expected dependency on η	55
31	Diffusion coefficients of different particle types measured via NanoPCS are constantly smaller than in DLS.	57
32	Diffusion coefficients of polystyrene nanoparticles measured in media with different ionic strength.	58
33	Gel mobility of DOPG-AuNRs shows successful functionalization and high stability. . .	64
34	Characterization of the nanosensors.	66
35	Mean diffusion coefficient and their standard deviation of the diffusors measured in dynamic light scattering.	68
36	Baseline autocorrelations without diffusors.	70
37	Control measurements for background scattering.	71

List of Tables

1	Diffusion coefficients from DLS and NanoPCS.	56
2	refractive indices for the glycerol/water ratios.	67
3	Measured viscosities for the glycerol/water ratios.	68
4	Diffusion coefficients for Au@mPEG, Au@cPEG and PS-NP determined via DLS.	69
5	Fitting parameters and claculated diffusion coefficients: Au@mPEG	72
6	Fitting parameters and claculated diffusion coefficients: Au@cPEG	72
7	Fitting parameters and claculated diffusion coefficients: PSNP	72

Part I

Introduction and Theoretical Background

Plasmonic Metal Nanoparticles

In the last 10-15 years nanotechnology got a prominent field in science and many developed products found their application in our daily routine from food to the automotive industry.[1] The biggest category where nanomaterials are used is the health sector, where silver is in fact the most frequently used metal. Walking through a drug-store we can get the impression that colloidal silver can cure any cosmetic problem within a week, long term effects are of course not reported yet. Nano-silver in bottles is also sold as medicine against Ebola, which might have the same scientific background as using silver bullets against werewolves and vampires except of the sad truth that Ebola really exists. Apart of these examples, there are also fields especially in biochemistry and biophysics, like sensing and imaging, where metal nanoparticles legitimate their use (to be fair with colloidal silver: it shows antimicrobial and antibacterial effects). After a quick overview on the general biomedical applications of metal nanoparticles, I will introduce the most important property of metal nanoparticles: Their plasmon resonance and its application in sensing.

Metal nanoparticles in biomedical applications

Metal nanomaterials are synthesized in a variety of sizes, geometries and with nearly all kinds of surface coatings. While metal oxide nanoparticles tend to react chemically with their environment, particles synthesized of noble metals, except of silver, count as chemically inert in biological media. Because of being inert and having a high surface to volume ratio noble metal particles, especially gold colloids and clusters, are versatile carrier systems.[2] By enduing them with recognition elements and certain therapeutics, drug delivery systems can be designed with defined metabolic destinations and limited cytotoxic effects.[3] As 'immunogold' gold nanoparticles coated with secondary antibodies are used as labels in electron microscopy, where they are visible because of their high electron density. The most important property of noble metal nanoparticles is their sharp spectral adsorption and scattering peak tunable over a large wavelength range from ultra-violet (UV) to near-infrared (NIR) light due to their localized surface plasmon resonance.[4] Especially metal nanoparticles with extinction in the NIR region can be used for *in vivo* therapies, as the penetration depth of light into skin is highest for a wavelength range between 650 – 1300 nm.[5] Thus extinction of light by a nanoparticle leads to localized heating of their environment and enables for example destruction of cancer cells.[6][7] Having a certain color, nanoparticles can also work as a colorimetric biomarker, when functionalized with a certain antibody or aptamer.[8] For all these techniques the extinction maximum, i.e. the apparent

color of the particles is considered as fixed. In reality adsorption and scattering maxima of metal nanoparticles are influenced by the nearby environment of the particle's surface, a phenomena that permits their usage as single particle sensors in biophysics and biochemistry.[9][10]

Theoretical basics of single localized surface plasmon resonance sensing

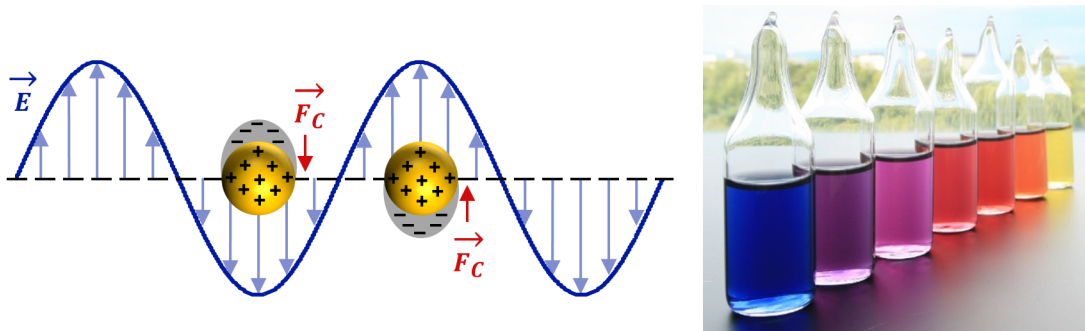


Figure 1: Plasmonic properties of noble metal nanoparticles. The conduction band electrons of metal nanoparticles oscillate when irradiated with light. A restoring force of the positively charged lattice ions, that do not move, damps the oscillation. Due to this effect the absorption and scattering of the particles is highest at a certain resonance wavelength, which is reflected by the color of the particles.¹

The colorful appearance of gold nanoparticles originates from their plasmonic properties. A localized surface plasmon is generated when a nanoparticle is irradiated with the electric field (\vec{E}) of light with a wavelength larger than the particle's diameter, which is in the case of gold in the visible wavelength range. If the size of the nanoparticles is small compared to the wavelength of the light the electric field can be assumed to be homogeneous over the size of the particles (quasi static approximation, QSA). The free electrons of the particles oscillate collectively with the electric field but with a restoring coulomb force (\vec{F}_C) of the positively charged lattice ions of the metal (Fig. 1) and a damping dependent on the polarizability α of the medium surrounding the particle. Damped oscillating systems correspond to a Lorentz-shaped peak in the frequency spectrum and have a resonance frequency, which is, translated to our plasmon, dependent on material, size, and geometry of the nanoparticle and most important for sensing on the refractive index of the surrounding medium ($n_m = \sqrt{\epsilon_m}$ with ϵ_m being the dielectric constant of the medium) . These relations can be demonstrated from the Mie-theory, describing the scattering cross section (C_{sca}) for a small spherical particle with a volume V and a wavelength dependent dielectric function of $\epsilon(\lambda) = \epsilon_1 + i\epsilon_2$ in a medium with ϵ_m by an analytical solution of Maxwell's equations. With some simplification described in [11] this scattering cross section of a small

¹Picture taken by Felix Mattick

spherical nanoparticle is quoted as[12]

$$C_{sca} = \frac{34\pi^4 \epsilon_m^2 V^2}{\lambda^4} \frac{(\epsilon_1 - \epsilon_m)^2 + (\epsilon_2)^2}{(\epsilon_1 + 2\epsilon_m)^2 + (\epsilon_2)^2} \quad (1)$$

The maximum of the scattering intensity is at the wavelength (λ_{res}), where the wavelength dependent real part of the dielectric function is $\epsilon_1 = -2\epsilon_m$, if the imaginary part of the dielectric function ϵ_2 is only weakly dependent on wavelength (which is not true for small spheres in medium with low refractive index). Thus a change the refractive index of the surrounding medium (Δn_m) shifts the resonance wavelength λ_{res} . The sensitivity S of a particle is described as the shift of plasmon resonance wavelength $\Delta\lambda_{res}$ upon a refractive index change Δn_m and is dependent on the type of particle.

$$S = \frac{\Delta\lambda_{res}}{\Delta n_m} \quad (2)$$

An extension to this theory for elongated objects was developed by Gans, who calculated the absorption and scattering cross-sections for ellipsoids with the result that a particle spectrum consists of two peaks (transversal and longitudinal).[13] The position of the longitudinal peak is dependent on a geometry factor L showing a dependency on the aspect ratio $AR = length/width$ of the particle well approximated by $L = (1 + AR)^{-1.6}$. [14] Thus with increasing aspect ratio of a nanorod the longitudinal plasmon resonance wavelength of the particle shifts to the red, while the absorption and scattering cross-section increases until a maximum is reached.[15] The scattering cross section of a particle is proportional to the square of the polarizability $C_{sca} = |\alpha|^2$, in QSA for a ellipsoidal particle defined by [11]

$$\alpha = V\epsilon_0 \frac{\epsilon_r - 1}{1 + L(\epsilon_r - 1)}$$

with the relative dielectric function $\epsilon_r = \epsilon(\lambda)/\epsilon_m$. Assuming a weak wavelength dependency of the imaginary part of $\epsilon(\lambda)$, the resonance condition is fulfilled when $1 + L((\epsilon_1(\lambda)/\epsilon_m) - 1) = 0$. The dielectric function ϵ_1 is described by the Drude model for a metal with bulk plasma frequency ω_p and a damping parameter γ and reads

$$\epsilon_1 = \epsilon_\infty - \frac{\omega_p^2}{\omega + \gamma^2} \quad (3)$$

With $\gamma \ll \omega$ and $\omega = 2\pi c_0/\lambda$, we obtain a dependency of λ_{res} on n_m for nanorods of [14]

$$\lambda_{res} = \lambda_p \sqrt{\epsilon_\infty + n_m^2 \left(\frac{1}{L} - 1 \right)} \quad (4)$$

Over small refractive index changes the increase in λ_{res} is linear with a factor (the particle's sensitivity S) mainly dependent on the geometry (aspect ratio AR) of the particle and being much higher than for spheres. The higher the sensitivity of a sensor, the higher the response ($\Delta\lambda_{res}$) of the sensor upon a refractive index change. With calculated adsorption spectra one can find an approximation for the dependency of λ_{res} on the refractive index of the surrounding medium for nanorods of:[16]

$$\lambda_{res} = (53.71 \cdot AR - 42.29) \cdot n_m^2 + 495.14 \quad (5)$$

To sum this section up, we can tune the 'initial' plasmon resonance wavelength of a nanoparticle used for sensing by synthesis (size, geometry and material) and predict the magnitude of the plasmon response this sensor will have on a refractive index change. Plasmonic metal nanoparticles change their resonance wavelength upon every event that influences their dielectric environment: binding of an analyte, distance changes between two particles, particle growth and charging. Since nanorods show a higher adsorption and scattering cross-section and a higher sensitivity compared to spheres they got more important for sensing applications.

Single Gold Nanorods as Sensors

Gold nanorods are very versatile sensors in biological media, in particular because of the easy tunability of their plasmon resonance wavelength reaching to the infrared. While shorter wavelength in the UV-range often affect biological components, infrared light can be useful to irradiate a particle in tissue. Except from *in vivo* methods gold nanorods are used as *in vitro* refractive index sensors for biophysical and biochemical questions, and recently also more and more in material science, e.g. to study the shrinking of polymers.[17] To sense small resonance wavelength shifts $< 2\text{ nm}$, the polydispersity of a nanoparticle sample and the resulting measurement error of an ensemble spectrum are too high to resolve these signals reliably. Thus taking single particle scattering spectra and compare each particle only with itself is a preferred method.[10] As depicted before, the sensitivity as well as the 'initial' resonance wavelength of a nanorod can be defined by synthesis.[18] Calculating the scattering spectra of a nanorod, whose size can be described as a cylinder with spherical shaped caps, or more complicated composites is not possible analytically, but has to be done by numerical calculations. A method to compute these calculations is the Boundary Element Method (BEM),[19] which will be described shortly in the next section. I will also give an overview on how these calculations (and approximations taken from them) help in designing a sensor having certain properties. Simulated data shown here was calculated by Dr. Andreas Henkel.

Approximating sensing parameters by BEM calculations

For equation (2) and (4) we assume that the 'bulk' refractive index of the whole medium surrounding the particle is changed. For sensing, however, very often this is not the case, we rather adsorb only a layer of analytes with a certain thickness filling only a fraction of the active volume. As the electric near field of a plasmon decays with distance from the particle surface, the particle's sensitivity is also distance dependent (Fig. 2a). This effect has to be taken into account when measuring adsorption of single proteins, thin layers or adsorption upon a layer around a particle. The spacial inhomogeneity of the near field enhancement over the particle's surface, being highest at the tips and lowest at the sides, can play a role in single molecule adsorption. Compared to other methods to simulate plasmons by solving Maxwell's equations, like Discrete Dipole Approximation (DDA) or Finite Difference Time Domain (FDTD), the MNPBEM (boundary element method for metal nanoparticles) toolbox for matlab was developed especially for metal nanoparticles and thus is less general.[20] Briefly, the particle is discretized by a mesh, whose size can be varied (Fig. 2b). The dielectric functions of the metal and the environment have to be set or they are taken from tabulated values. After specifying how the particle is embedded in its dielectric environment, for example that it is surrounded by a shell with ϵ_{shell} in a medium with ϵ_{medium} , scattering and adsorption spectra can be calculated (Fig. 2c). These

calculations can also be done for different excitation schemes, which gets important for anisotropic particles.

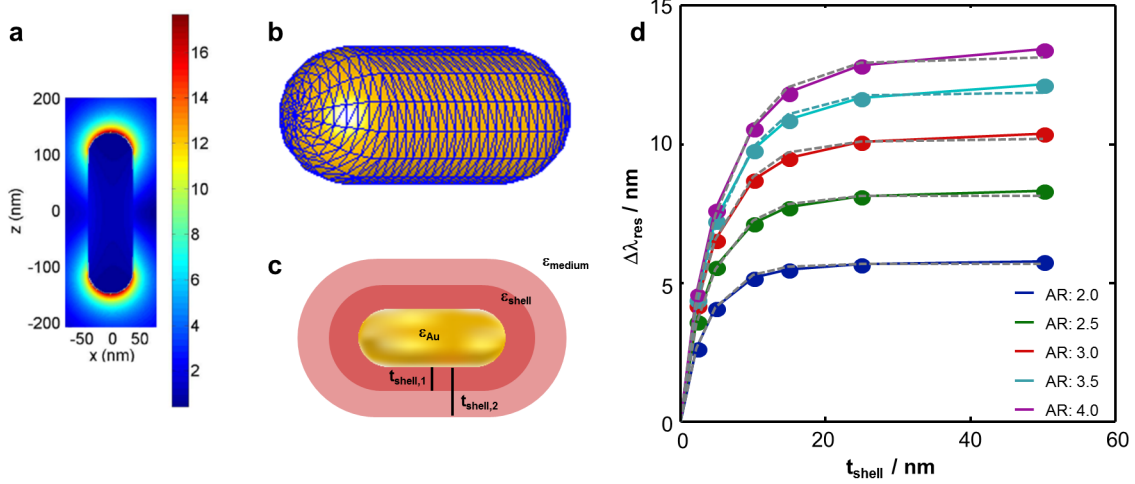


Figure 2: Calculating the sensing parameters for gold nanorods. a) The electric near field is enhanced inhomogeneously around the nanorod, is highest at the tips and decays with distance from the nanorod's surface.² b) For BEM simulations the surface of the nanorod has to be discretized. c) For simulations the geometry how a particle is embedded in its dielectric environment has to be given. Here shells with a thickness t_{shell} and a dielectric constant ϵ_{shell} around the particle are simulated. d) Plotting the resonance wavelength shift $\Delta\lambda_{res}$ against increasing shell thickness, shows an exponential increase, whose maximum wavelength shift is dependent on the aspect ratio of the nanorod. Figure d taken from Dr. Andreas Henkel.

Simulating shells with discrete sizes around the particle shows that the plasmon resonance wavelength shifts exponentially with shell thickness t_{shell} and a maximum defined by equation (2) $\Delta\lambda_{max} = S\Delta n$ (Fig. 2d). Fitting this data, the distance dependent wavelength shift can be calculated by

$$\Delta\lambda = S\Delta n \left(1 - e^{-\frac{t_{shell}}{d_s}}\right) \quad (6)$$

where Δn is the refractive index change, S the particle's sensitivity and d_s the decay length of the sensitivity, the so called sensing distance. S and d_s are parameters dependent on the nanoparticles geometry and size. Calculating these parameters for particles with different width w as well as different aspect ratios AR and relating them to their geometry (for S) and their volume (for d_s) we end up with two approximations (Fig. 3):

$$S \sim 114 \cdot AR, \quad d_s = 0.37 \cdot V^{\frac{1}{3}} \quad (7)$$

²<http://mappingignorance.org/2013/02/11/quantum-kisses-between-optical-nanoantennas;> (2016-05-25)

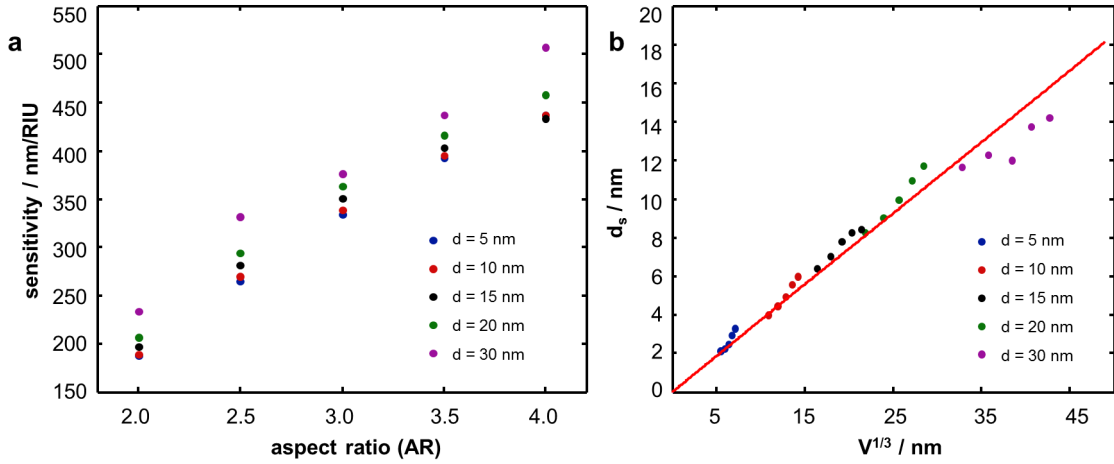


Figure 3: Relating sensitivity and sensing distance to particle geometries. a) Sensitivities calculated for particles with different aspect ratios and different volumes show a linear dependency on the aspect ratio. b) The sensing distance is linearly dependent on $V^{1/3}$.

with $R^2 = 0.92$ for S and $R^2 = 0.95$ for d_s . While the sensitivity increases with higher aspect ratio of the particle with a small offset dependent on the particle's diameter, the sensing distance increases with particle volume.

For these calculations a dense layer of a certain dielectric is simulated around the nanorod. In reality we are very often more interested in the shift a single protein would induce during attachment. Single protein detection requires a careful sensor design, as in general the shifts induced by single protein are smaller.

Theoretical calculations help for sensor design

The first criteria when designing a nanoparticle for sensing is the method, with which an analyte should be identified. For Surface Enhanced Raman Spectroscopy (SERS) for example particles with many edges (e.g. nanostars) are required as they are known to have hot spots of electric field enhancement which enhance the signal in several orders of magnitude.[21] For dark-field micro-spectroscopy measurements of single particles in a flow-cell, we have cameras taking scattering spectra in the visible wavelength regime between $500 - 800 \text{ nm}$. Following equation (5) the particles should not exceed an aspect ratio of $AR = 2.5$, so that the resonance wavelength is still measurable. Experimental data showed that particles with aspect ratio up to $AR = 3$ can be measured.[22] To be detected by the camera the particles need a certain scattering intensity, which can be mainly influenced by the volume of the particle ($C_{sca} \propto V^2$). The lowest limit experimentally determined for our routine setups with standard measurement parameters lies at a volume of $V = 6000 \text{ nm}^3$, which corresponds to particles

with dimension of $15 \times 40 \text{ nm}$. The scattering intensity can also be influenced by the light source and some measurement parameters, which will be discussed later. Within these borders a sensor can be synthesized being optimal for the size of a detected analyte and the number of analytes that should be sensed, i.e. single analyte adsorption or a concentration dependent coverage to determine binding affinities.

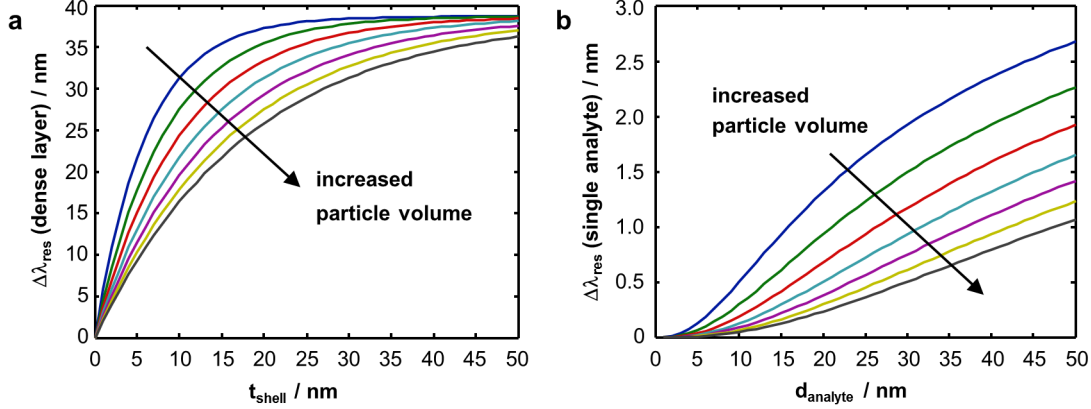


Figure 4: Dependency of $\Delta\lambda_{res}$ on sensor size. a) For a layer with a certain thickness t_{shell} the shift gets smaller for bigger particle volumes. However, particles with smaller volumes can not identify increase in shell thickness from a certain distance on as they already reached their maximum. b) Shifts a spherical single analyte with a certain diameter $d_{analyte}$ would induce show the same behavior.

The shift induced by a whole layer formation around a particle is given by equation (6). At a fixed aspect ratio an increased volume of the particles shows a reduced shift for a layer with a certain thickness (Fig. 4a). The shift induced by a single analyte can be calculated from this formula as well, ignoring the inhomogeneity of the electric field enhancement across the nanorod's surface, that causes different shifts on single analyte adsorption depending on the position where the analyte attaches (tip or side). This effect is reported to be negligible as a good approximation.[23] Assuming a dense layer of analytes with a layer thickness defined by the size of the analyte (e.g. its diameter $d_{analyte}$) and with refractive index $n_{analyte}$ around the particle, we can divide the shift this layer would induce by the number of analytes that would fit in the volume of this layer $N_{analytes} = \frac{V_{layer}}{V_{analyte}}$. [24]

$$\Delta\lambda_{single} = S\Delta n \left(1 - e^{-\frac{d_{analyte}}{d_s}}\right) \cdot \frac{1}{N_{analyte}} \quad (8)$$

Calculating the shift of a spherical single analyte with a certain diameter $d_{analyte}$, we can see the same behavior as for dense layers (Fig. 4b): The shift is smaller with increasing particle volume and thereby increased sensing distance (d_s). With the help of these calculations one could state that small sensors should be preferred, but if adsorption of a single analyte takes place upon a layer around the particles

(e.g. a layer of receptors), which is the normal case, the thereby increased distance of the analyte from the surface has to be taken into account.

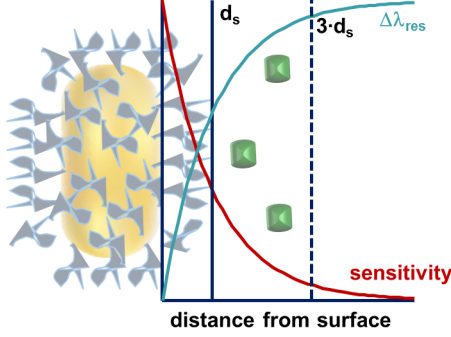


Figure 5: Sensing distance and sensor design. The sensing volume of a particle, the volume containing the refractive index sensitive environment of the particle, can be defined as the volume containing 63% of the particles sensitivity. Therefore it is given mathematically by the decay length of the sensitivity from the surface d_s . A sensing volume containing 95% of the sensitivity is defined by a distance of $3 \cdot d_s$ from the surface. If the sensing volume of a particle is already occupied by a recognition element adsorption of an analyte can not be detected anymore.

Knowing the size of the recognition element and the size of an analyte whose adsorption should be detected helps to design the sensor. If this recognition element already fills the sensing volume V_S , the volume that contains the refractive index sensitive surrounding of the nanorod, analyte adsorption can not be detected anymore. For analytes having high refractive indices or particles with high sensitivity we can assume a sensing volume containing 95% of sensitivity and thus mathematically being defined by a distance around the particle of three times the sensing distance ($3 \cdot d_s$).[24] However, the volume defined by the decay length of the sensitivity d_s which contains 63% of the sensitivity of a nanorod can normally be taken as a good approximation for a border when calculating the best sensor geometries, the adsorption of an analyte outside from d_s can not or only hardly be detected anymore (Fig. 5). Whether a passive layer around the nanorods has an impact upon the shift of further adsorbing analytes is still not clear. Investigating the distance dependency of adsorption and comparing the results with theoretical calculations, like the here discussed BEM simulations is still a field that has to be studied more.

State of the Art: Refractive Index Sensing with Dark-field Microscopy

The first ultra-microscope to visualize colloids below the diffraction limit was developed over 100 years ago by Siedentopf and Zsigmondy.[25] Scattered light of single nanoparticles could be observed perpendicular to the direction of the light beam. A similar principle is used in dark-field illumination, where the sample is illuminated with a hollow cone of light in such way that direct light misses the objective and nanoparticles are visible as colorful scattering centers on a dark background. This technique can be used for imaging or tracking of particles, or if coupled to a spectrometer for sensing applications taking advantage of the sensitivity of a plasmonic nanoparticle to its nearby environment described above. Dark-field microscopy with nanoparticles is even used in life cell cultures[26] here nanoparticles can be simple markers[27] or the investigated species, as their fate after uptake is a very important issue in drug delivery and nanoparticle cytotoxicity.[28] Going down from complex cells to proteins, a variety of techniques exist using dark-field micro-spectroscopy on single nanoparticles to investigate the biophysics of protein interactions or to develop sensor platforms for medical diagnostics.[9] Also for basic research on plasmon theory single particle spectra taken with this technique are important.[29] From the variety of applications I will go into detail for those that are the basic for my work.

Multiplexed plasmon sensors

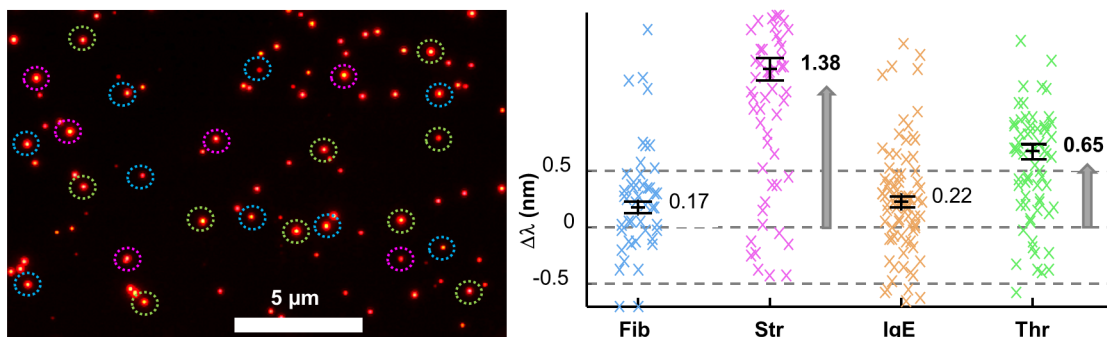


Figure 6: Multiplexed plasmon sensors. Particles with different functionalizations each specific for a protein are immobilized on a flow-cell surface and their position is recorded. Flowing in one or more analytes the particles show specific binding affinity to shows a shift in plasmon resonance wavelength of the specific particles. Figure adapted from [30]

A multiplexed plasmon sensor is a device which can find its application in point-of-care diagnostics for rapid and label-free detection of pathogens. To proof the feasibility of this kind of sensors, particles

were functionalized with different aptamers each responding specifically upon binding of a certain protein. These sensors are randomly deposited on a flow-cell surface and their position is recorded. The presence of one (or more) of the analytes, the particles are sensitive to, is detected in a shift in the plasmon resonance wavelength of the particles (Fig. 6).[30] The advantages are obvious: First of all the technique is label-free, no time-consuming or defective labeling steps have to be performed. Furthermore the sensor preparation is easy as the particles are deposited randomly. Last but not least, the whole procedure is cost-efficient as measurements can be done on a normal microscope setup equipped with a dark-field condenser and a camera. The proof-of-concept was done for a system with four different analytes, however, upscaling is not a straight forward process. The higher the number of analytes and receptors, the higher the possibility for unintentional cross-talk, i.e. unspecific binding. Further the measurement time increases, the higher the number of particles on the sensor surface, as particles are scanned one by one. A fast measurement time would only be possible at the expense of statistics. The latter problem can be solved by single wavelength measurements,[31] a principle where the intensity-change at a certain wavelength upon plasmon shifting is measured and which is explained further in this work. The problem of a cross-talk can be solved by constructing sensors, that exclude already a certain kind of analytes for example by size. A sensor coated with a porous material as it is in case of silica with a certain pore size can be suitable to give access to the sensor surface only to analytes below a certain size. This principle is already used for SERS-sensors.[32]

NanoSPR sensors to quantify multiple protein-protein binding affinities

Going beyond simple detection of an analyte also its binding affinity to a receptor can be determined in a multiplexed way.[33] In biochemistry protein-receptor interactions are very often characterized by genetic modification of the receptor or the protein and quantification of the influence of the modified region on the binding affinity. It was shown that by functionalization of particles with differently modified receptors, all binding partners for a common analyte, the binding affinities between the analyte and all receptors are quantified simultaneously. These experiments were extended in all directions: Measurements were done in presence of an inhibitor, changing buffer, or adding a salt to investigate its influence. In nature exists a variety of proteins that are able to form higher ordered oligomers, whether with other proteins or biological components or with themselves. For many of them the reactive species is not yet identified. As a nanosensor approaches the size of a protein and the shift of a single protein can be calculated, our sensors give the opportunity to not only determine binding affinities, but also identify the reactive species in a multi component analyte mixture. A principle that is shown in this work.

Diffusion sensing and determination of surface interactions

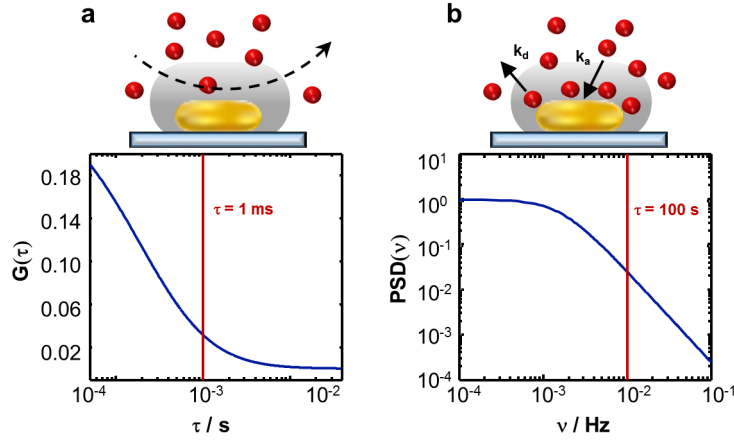


Figure 7: Diffusion sensing and surface interactions. a) If interactions between particles in solution and the nanosensor are negligible, the particles diffuse through the sensing volume of the nanosensor with a diffusion time τ_D in the millisecond regime. This diffusion time can be taken from the autocorrelation of the fluctuating resonance wavelength of the sensor over time and is dependent on the size of the sensing volume. b) If interaction between particles in solution and the nanosensor surface play a role the sensor gets covered with a fluctuating coverage density of analytes in equilibrium. The time scale of these fluctuations, evaluated *via* the power spectral density (PSD) is much slower than for pure diffusion and is dependent on the binding constants of the interacting system. With $\tilde{k}_a = k_a \cdot c = 7.85 \cdot 10^{-6} \text{ s}^{-1}$ and $k_d = 0.01 \text{ s}^{-1}$, which are typical rate constants, we get $\tau = 100 \text{ s}$.

To measure the adsorption of single proteins a setup was used, where a time resolution of 10 ms was achieved. It was possible to identify the adsorption of single protein binding events taking place at the millisecond time scale as shift in plasmon resonance wavelength.[34] This special dark-field setup, which will be characterized in the next section, was still not used to full capacity concerning its time resolution. Tuning this setup further, opens up for measuring events on even higher time scale, e.g. diffusion. A particle is diffusing through a medium until it gets adsorbed at a surface with a rate constant for adsorption k_a and later desorbed again with a rate constant for desorption k_d . If the binding affinity is sufficiently low, we can neglect interactions and the particle passes the sensor without attaching. To be still sensed as present in the sensing volume of a nanorod it has to come close enough to enter the sensing volume and measurements have to be sufficiently fast compared to the diffusion time of the particle. Getting an understanding on how pure diffusion of particles close to the nanosensor surface without any interactions can be sensed is the first step to later determine diffusion that is influenced by surface interactions. These surface interactions can be weak attractive or repulsive interactions or stronger interactions like binding. Diffusion takes place at high frequencies

(> 100 kHz), with diffusion times of $\tau_D < 1 \text{ ms}$, for a particle crossing a nanoscale area. Analyte binding to a surface leads to a fluctuating surface coverage with fluctuation frequencies dependent on the kinetic rate constants $\tau^{-1} = (4 \cdot \tilde{k}_a + k_d)$, where \tilde{k}_a is a concentration dependent rate constant ($k_a \cdot c$). For typical kinetic rate constants one can obtain a frequency of $\tau^{-1} = 0.01 \text{ Hz}$, which corresponds to a time regime of $\tau = 100 \text{ s}$. [35] The stronger the binding, the lower the frequency τ^{-1} . To measure systems with stronger binding affinities, a setup with high stability on the long time scales is required. As for this work diffusion was measured, a process that happens on small time scales, I modified and characterized a setup to be suitable for measurements of fast dynamics.

Overview

In the following main part of this thesis, I will first introduce the microscope setups used and the improvements and characterization made on one of them for diffusion measurement. I will show that silica coated gold nanorods are suitable particles to investigate the sensing behavior of gold nanorods experimentally and on single particle level. Additionally, because of the porous nature of the shell, these particles are sensors having a molecular weight cut off for analytes trying to access the gold surface. A principle that can help in upscaling multiplexed sensing, as the sensor can make a preselection of analytes which could reduce unspecific interactions. With the help of IM30, an oligomer forming protein, I proved that apart of determining the binding affinity we are able to identify the adsorbed species of the protein (protomer or oligomer) taking advantage of the small sensor size. Finally as main part of my work, I was able to measure diffusion of particles through the sensing volume of our nanorods with the beforehand improved microscope setup and to quantify the influence of the viscous drag caused by the surface of the sensor and the flow-cell. The measurement of pure diffusion in the particles environment is the first step to determine surface interactions.

Part II

Sensing with Single Plasmonic Gold Nanorods - New Methods

Dark-field Micro-spectroscopy Setups: Measuring Fast Dynamics Requires High Time Resolution

Abstract

Single particle spectra were already taken years ago,[36] since that time setups were improved and automatized a lot. In this work different types of measurements on single gold nanorods were performed. First of all static measurements, where the particles are measured before and after for example a change of the medium they are measured in. The time resolution for these measurements is not the important parameter as the mean response in plasmon resonance wavelength shift for all particles should not change during measurement, most crucial is the spectral precision that ensures a good repeatability of the measurements. The dark-field microscope setup to perform these measurements is already build, characterized and well established. However, to measure fast dynamics, as the diffusion of an analyte in the sensing volume of our particles, we need a microscope setup with a high time resolution combined with a high stability over the length of the measurement. Measuring time traces at high time resolutions means that a certain sampling rate is reached fast and allows for relatively short measurements. To obtain a spectrum at low exposure times a light source with high photon density is needed, e.g. a white-light laser. A prototype of this setup was already build and measurements were also done,[34] but not at the limit of the possible time resolution. Since measurements in our group are done with a self-written software ('Nanocenter') allowing to proceed a whole measurement from there, it was also an aim to implement the changes that have to be made for the measurements of fast dynamics in this software. The setup was rebuild for laser safety requirements and I characterized and improved the stability concerning noise in the high frequency range as well as for measurement repeatability. Further, measurements can now be done with a slightly modified 'Nanocenter'-software, making the whole procedure more user-friendly and less time-consuming.

Routine setup and total inter reflection (TIR)-setup

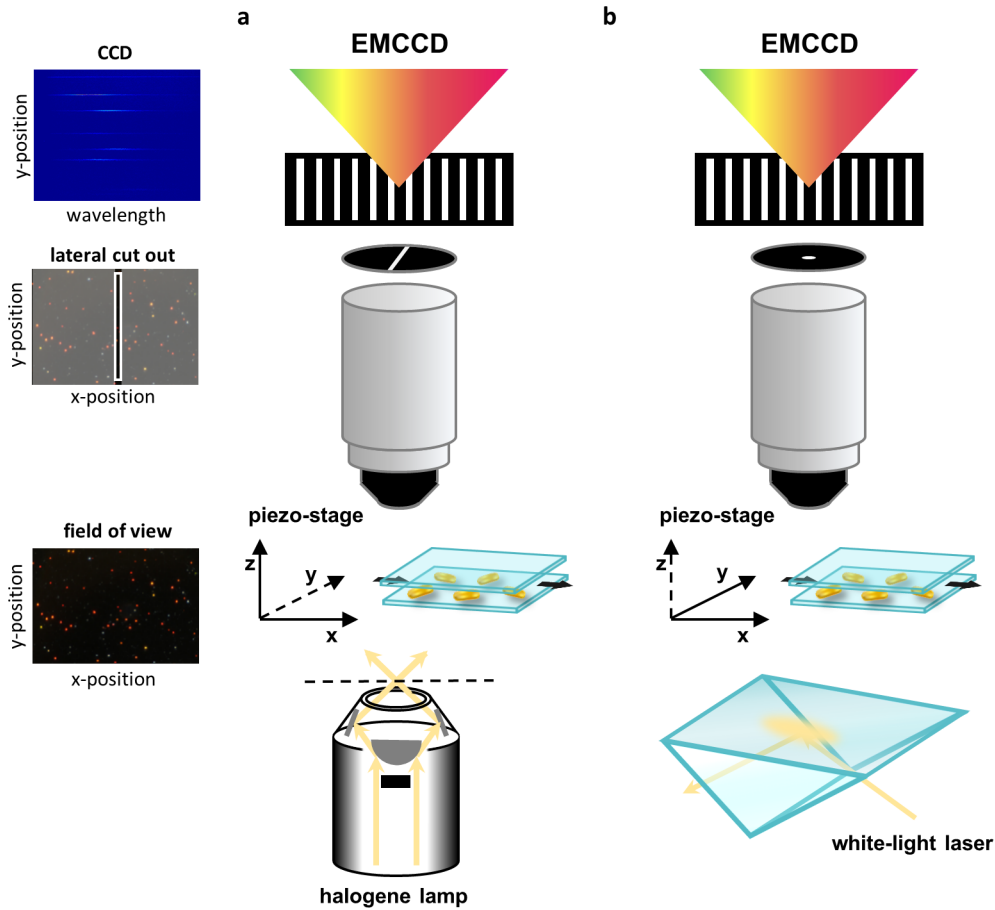


Figure 8: Scheme of the two different setups. a) Routine-setup: The sample is illuminated with a dark-field condenser. The particles are centered via a x-y-piezo stage. A slit placed in the light-path cuts out all light in x-direction except from the particle directly centered. The particle spectra are detected on an EMCCD-chip after being spectrally resolved by a grating. b) TIR-setup: An evanescent field generated on the flow cell surface via a prism excites the particle plasmon. The particles are centered in x- and y-direction under the microscope objective and passed through a pinhole, so that only light from one particle is spectrally resolved and detected on the EMCCD-chip.

The measurements in this work were done on two different setups, on the one hand on a routine refinement setup and on the other hand on a setup where spectra from one particle can be measured with high time resolution (hereinafter referred to as total internal reflection TIR-setup). At the routine setups, the requirements are to scan many particles with high spectroscopic precision and high

repeatability in ideally a short time to compare small changes in resonance wavelength from one measurement to the other. The routine setup (Fig. 8a) and its capabilities were described previously.[30] The nanorods immobilized in a microfluidic flow-cell are illuminated by a halogen lamp via a dark-field condenser. While direct light misses the objective of the microscope, scattered light from the sample is captured. With a $50\ \mu\text{m}$ broad slit in the image plane of the light path only the light from particles directly centered under the objective passes and is spectrally resolved. Thus we get again a two dimensional picture on the CCD-chip of the camera, with on the y-axis showing the local position of the particles and on the x-axis the wavelength of the light coming from the particle. Briefly, we get high repeatability by centering each single particle laterally and focally at each measurement in ideally the same way under the objective. In x-direction we move the sample via a piezo stage, in y-direction this stage is not moved, but the cut out of the respective spectrum from the CCD-image is done by software. The focusing in z-direction is also done with a piezo-device moving the objective of the microscope until highest scattering intensity is reached indicating optimal focus position. The time for one measurement is finally set together by the number of particles selected in the field of view, the time we need to center the particles (refinement), the exposure time and the number of spectra taken for averaging. This procedure ensures a high repeatability of the measurements, because of the high spectroscopic precision with which we measure every single particle.

To measure fluctuations of single particle plasmon resonance wavelength with high time resolution the requirements to the setup differ slightly (Fig. 8b). These measurements are done by centering a single particle once and measure than with high time resolution. Here fast refinement is convenient but not necessary for measuring a time-trace. Although a proper refinement is aspired, it is not necessarily needed for the signal, but rather for a better signal-to-noise ratio as the scattering intensity is highest for a focused particle. To capture the scattering spectra of a particle with high time resolution, meaning with short exposure times, we need a light source with high photon density, in our case a white-light laser, a camera with the possibility for a fast read out and a mechanically very stable setup. As measurement principle, the sensor particle is excited by the evanescent field of a white-light laser coupled into a prism in total internal reflexion (TIR) geometry. In contrast to the routine setup the particle is centered in x- as well as in y-direction beyond the objective with a piezo stage. Focusing is done by moving the objective via a stepper motor and thus less precise than with a piezo-device. To make sure that only light from one single particle is illuminating the camera chip, we pass the light through a pinhole instead of a slit. The camera, the light source and the improvements in setup stabilization and measurement repeatability are explained in more detail in the following sections.

Fast measurements are mainly possible because of camera settings

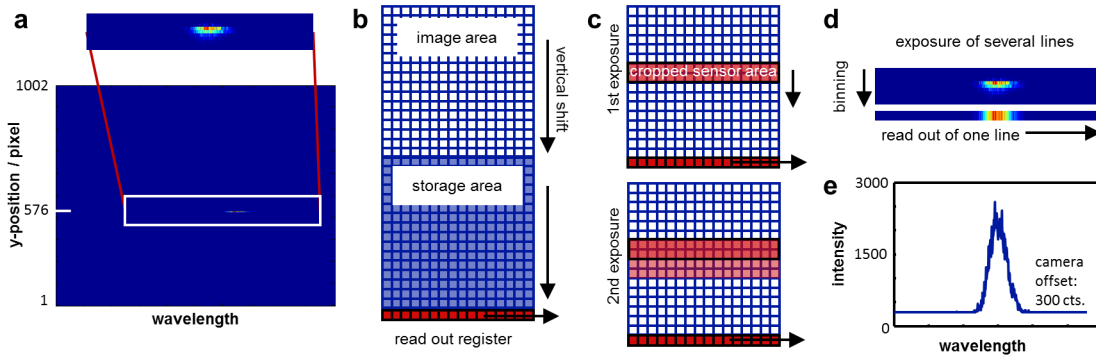


Figure 9: Camera settings that enable fluctuation measurements. a) Passing the scattered light through a pinhole ensures that only light from one particle reaches the camera chip. With a fixed pinhole the CCD-chip is illuminated always at the same y-position, the x-axis reassembles the wavelength. From the picture we can see that at an exposure time of $60 \mu\text{s}$ no background light is detected. b) Frame-transfer mode: The camera chip consists of two parts having the same size: The image area, which is illuminated and the storage area sitting between the image area and the read out register and which is covered by an opaque film. Both areas can be shifted independently. c) Crop-mode: The sensor is cropped to the number of lines that are illuminated and only this number of lines is shifted for the next exposure. d) Vertical-Binning: As all rows contain the information from one particle, they can be summed up in the read out register and read out as one line. e) The resulting spectrum shows the camera offset of 300 *cts*.

The possibility for fast measurements at the TIR-setup are technically given by the EMCCD-camera (Andor iXon DV885). The camera has a two dimensional chip, where in our case the vertical dimension is defined as the local position of the pinhole under the CCD-chip, and the horizontal dimension is the spectral resolution of the scattered light (Fig. 9a). After exposure of the camera chip to light, charge is induced and has to be shifted vertically to the read out register, from where each horizontal line of pixels is read out consecutively. As the read out of the chip from the read out register is time-consuming and has to be done before the chip is illuminated with the next spectrum, the camera has a special frame-transfer mode. For this property the CCD-chip contains an image area and a storage area of the same size, that sits between the image area and the read out register (Fig. 9b). While the image area is exposed to light, the storage area is covered by an opaque film. The possibility to shift these areas independently from each other allows shifting a spectrum taken in the image area into the storage area. From the storage area the image is read out while the next image is already taken. The exposure time is then limited by the read out time from the storage area. As we block all background light that is not coming from a particle centered under the objective of the microscope, we do not illuminate the whole chip of the camera, but only several lines. By cropping the camera chip to this number of lines,

one can decrease virtually the sensor size and read out much faster, as only a decreased amount of lines has to be shifted. The empty lines that lie above the illuminated ones move up and get exposed with the next spectrum (Fig. 9c). As the illuminated lines are in our case in the middle of the chip, we have to choose the number of lines cropped that way, that we do not cut the spectrum in the middle. A number of 10 lines was found to not showing any overlaid pictures. Therefore, the first frames that we obtain are empty until the first spectrum reaches the read out register. All horizontal lines of a cropped sensor contain the information from one single particle spectrum, so that we can simply sum them up in one row, which is called binning (Fig. 9d). All charge from these lines is shifted together into the read out register and processed afterwards. Thus the time consuming read out step is reduced to one and the circular buffer of the camera is filled with only one row of pixels per spectrum instead of several. Because of a camera offset we get a spectrum with an offset of 300 *cts* (Fig. 9e). The camera has an intrinsic cleaning cycle starting after every 400,000 frames, which limits the total measurement time at a certain exposure time. I included all these features in the 'Nanocenter'-Matlab software, that is used to conduct the whole experiment, and are now automatically set when time-traces are measured. Apart of the technical possibility of reading out the camera with high frequency for a single nanoparticle spectrum it has to be ensured that the light reaching the camera in such short exposure time is high enough to be recorded as a sufficiently stable signal.

Super continuum white-light laser is a suitable light source to achieve high photon density

The other key part for the TIR-Setup that makes fast measurements possible is the light source, a super continuum white-light laser (Koheras SuperK Power). This 5 *ps* pulsed laser has a wavelength range from 460 – 2400 *nm* with a total average output power of > 2800 *mW*. Since our particles scatter in the visible wavelength range and we do not want unintended heating from infrared light we filter out the NIR-/IR-light (> 800 *nm*). The total visible power of the laser is still > 300 *mW* with a spectral power density from 470 – 670 *nm* of 1 *mW/nm*. A typical normalized white-light spectrum a white scatterer (silica particle) taken with the TIR-setup reflecting the spectral distribution of the laser light intensity combined with the detector sensitivity is shown in Fig. 10a. Light with wavelength above 800 *nm* is filtered out and the quantum efficiency of the camera is highest (>50%) between 450 – 780 *nm*, which in combination leads to the shown spectrum. To use the laser to full capacity particles with a plasmon resonance wavelength between 600 – 700 *nm* should be applied as sensors. Measuring the fluctuation of the laser intensity at one single wavelength for 20 *s* demonstrates that the laser intensity fluctuates randomly and equally for all frequencies as can be seen in the power spectral density (Fig. 10b) and the autocorrelation (Fig. 10c) of the measured intensity. The standard deviation of the intensity measured over 20 *s* with a frequency of 20 *kHz* is $\sigma = 0.0022$ *cts*. In contrast

to the illumination with a halogen lamp, the temporal coherence of the laser can induce interference artifacts if the setup is not sufficiently stable, e.g. because of mechanical vibrations.

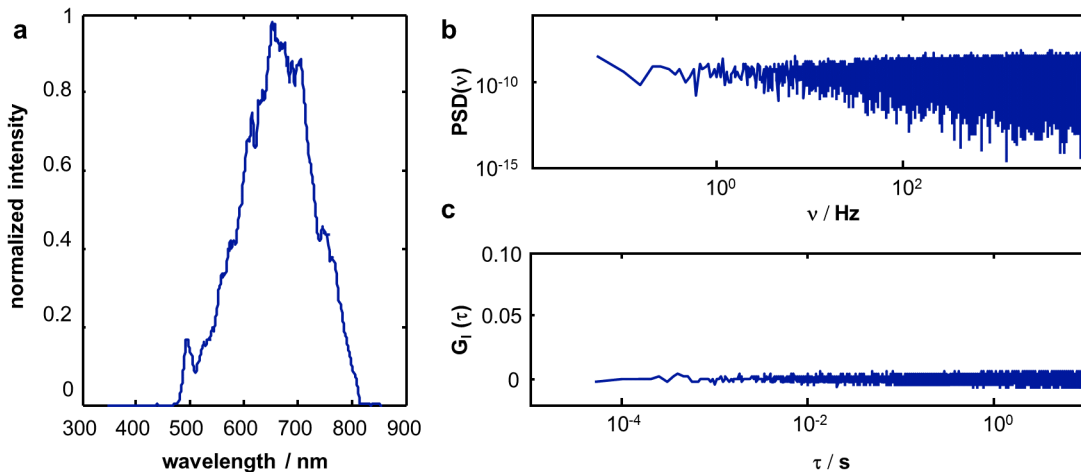


Figure 10: Spectral distribution and stability of the laser intensity. a) The normalized intensity of a white-light spectrum from a silica-particle shows the spectral distribution of the laser intensity combined with the camera sensitivity and is highest between 600 – 700 nm. b) The power spectral density shows a stable laser signal for all frequencies. c) The autocorrelation of the laser intensity confirms random fluctuations.

Setup improvements for higher stability and better repeatability

Since I showed that the laser intensity fluctuates randomly, all oscillations in the plasmon resonance wavelength, as well as in the intensity are coming from instabilities in the setup, mainly, as we are talking about oscillations from mechanical vibrations. To reduce these artifacts and stabilize the setup, the whole microscope setup (Zeiss Axiovert) is mounted on an optical table damping all vibrations coming from the outside (building, walking around). The piezo-stage, where the flow-cell holder is inserted is mounted on a heavy steel-plate independently from the microscope stand. Important is that all components that could cause vibrations, e.g. controllers or fans, are either switched off or placed independently from the optical table. The CCD-camera has the possibility to cool the peltier-device, that is cooling the camera chip by water cooling instead of the usually set fan, which gave a big increase in stability. A very crucial part, if malfunctioning, is of course the piezo stage. A sudden regulation in position by the feedback-loop because of dirt in the cleft of the stage can be disturbing, as reflected in the time trace (Fig. 11a). After stabilizing the setup I was able to obtain autocorrelations of the signal that do not show any correlated noise (Fig. 11c).

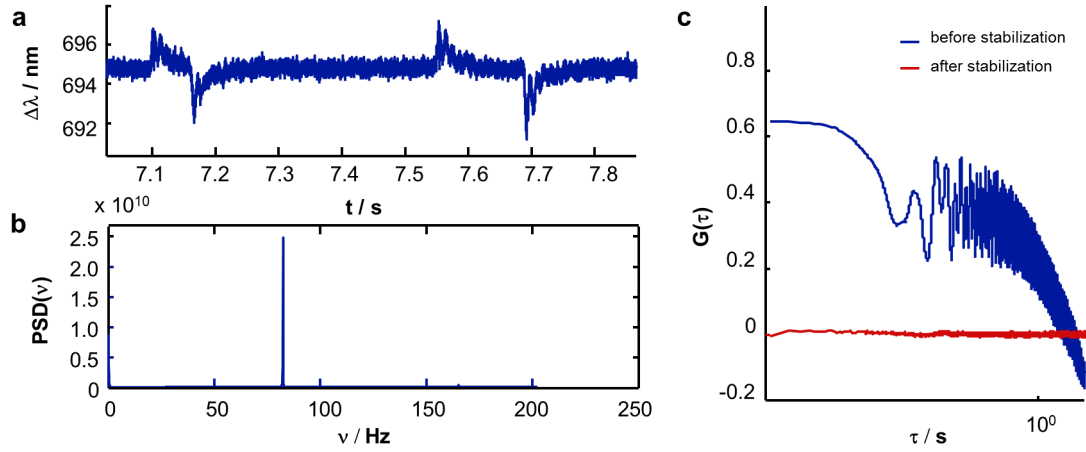


Figure 11: Setup stabilization. a) Resonance wavelength over time measured with a malfunctioning piezo-stage. The movement of a few nanometers can disturb the signal stability significantly. b) Power spectral density where the impact of the vibration of the camera fan is shown at a huge peak at around 80 Hz. c) Autocorrelation before and after setup-stabilization. After stabilization the signal fluctuates completely randomly.

For the repeatability of the measurements, we have to ensure a proper refinement of the particle. For the refinement, we scan once over the particle and detect the intensities at each position. The center of the particle is assigned to the position with highest intensity, thus the stage goes back to that point. This way of refinement is done for lateral centering of the particle via the piezo-stage, but in z-position via a stepper-motor. This motor has the disadvantage that with changing the direction, we have a hysteresis of the position. Going back to the position where on the way forth was the highest intensity, does not mean to hit the focus of the particle (Fig. 12a). To focus the particle properly, we have to scan in one direction, go back and direct the focus position always from the same initial point. By doing that, we achieved a repeatability for the measurements of $\lambda = 0.3 \text{ nm}$ (Fig. 12b). For this measurement two different particles that are positioned as far from each other as reachable by the stage were measured during 4 circles successively. The correct focusing is not only important for the repeatability of the measurement, but also for a better signal to noise ratio.

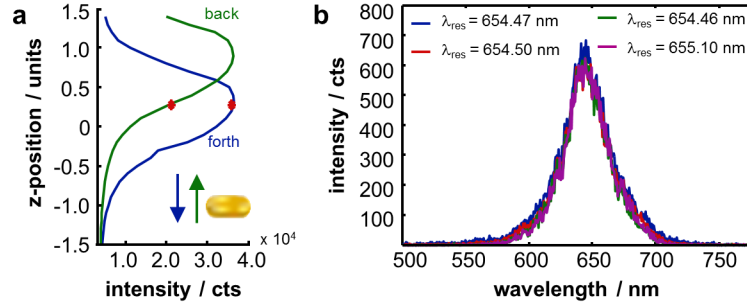


Figure 12: Improving precision of focusing to obtain better repeatability. a) To determine the focal position, the intensity of the particle is detected at different z -positions on the way forth. On the way back we have to overcome a hysteresis in position setting by approaching the particle always from the same direction. b) Repeatability measurement shown for one particle. The measured spectra have intensity variations of less than 10% and a repeatability for λ_{res} of $\delta\lambda_{res} = 0.3 \text{ nm}$.

Noise dependency on scattering intensity

For our fluctuation measurements, it is interesting to know the influences of our camera settings (exposure time t_{ex} and gain) on noise. Noise in our case is defined as the standard deviation of the plasmon resonance wavelength fluctuation (σ_λ) measured over a certain number of frames (Fig. 13a). To check if the exposure time has an influence on noise, or if noise is just dependent on the scattering intensity of a certain particle (I_{res}), two types of particles with different sizes that have similar intensities at different exposure times were measured with the same number of frames:

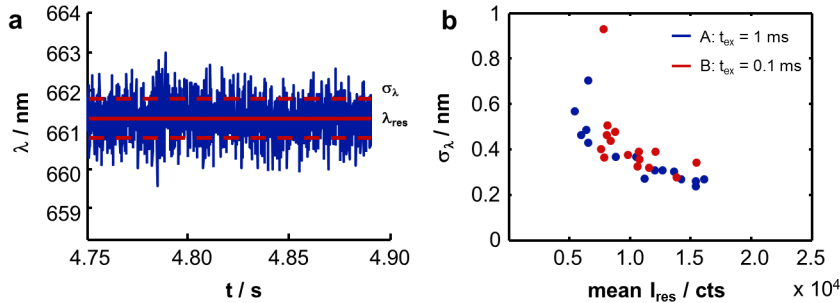


Figure 13: Noise dependency on exposure time. a) Noise for a fluctuating signal is defined as the standard deviation of λ_{res} over the measured time-trace. b) Two types of particles of different sizes were measured at different exposure times but with the same number of frames: A (ca. $30 \times 70 \text{ nm}$) at $t_{ex} = 1 \text{ ms}$; B (ca. $50 \times 100 \text{ nm}$) at $t_{ex} = 0.1 \text{ ms}$. Increasing the exposure time does not lower noise, if the scattering intensity (I_{res}) of the particles stays constant.

- Type A: (ca. $30 \times 70 \text{ nm}$); $t_{ex} = 1 \text{ ms}$; measured time: 100 s (100,000 frames)
- Type B: (ca. $50 \times 100 \text{ nm}$); $t_{ex} = 0.1 \text{ ms}$; measured time: 10 s (100,000 frames)

It can be clearly seen that noise is not dependent on the exposure time, but on the intensity of the particle itself (Fig. 13b), indicating that our measurements are shot noise limited. The more signal we have the smaller the influence of shot noise. If we want to measure at high time resolution and decrease the noise of the signal, we have to use bigger nanorods or nanorods with increased aspect ratio as sensors, as the scattering cross-section of a nanorod is dependent on their volume $C_{Sca} \propto V^2$ and a geometry factor.[12] For many experiments and measurements, the size and geometry of the sensor has to be chosen considering the size of the analyte. Roughly we can say that the smaller the analyte the smaller the sensor should be to have a sufficient sensitivity. Hence increasing the sensor is not always an option. To increase the intensity of the spectrum taken at a certain exposure time, that is read out from the camera, we can increase the gain settings.

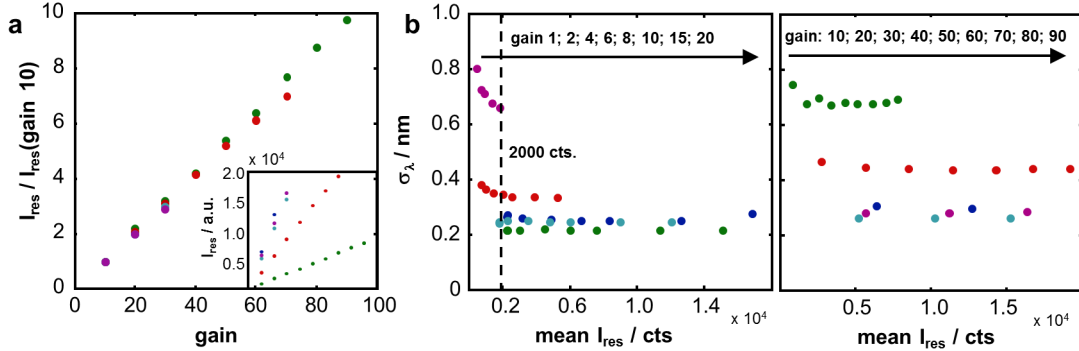


Figure 14: Effect of an increased gain on noise. a) The normalized scattering intensity ($I_{res}/I_{gain\ 10}$) of a particle is increased linearly by the factor with which we increase the gain. Inlet shows the not normalized I_{res} . b) At higher particle intensities (right) increasing the gain does not have an effect on the noise of a certain particle, if we measure particles with lower intensities (left), however, we can see that below an threshold of 2000 cts we can decrease noise by increasing the gain (each color indicates a single particle).

We measured the noise for particles of type B at $t_{ex} = 60 \mu\text{s}$ for increasing gain from 1 to 90 (or until a certain particle overexposed the camera). Normalizing I_{res} to I_0 that I defined here to be the intensity at a gain of 10 we can see, that the intensity is amplified linearly by the factor we increase the gain (Fig. 14a). Although an increasing gain shows a linear amplification of the intensity, noise is only reduced when our particle has an intensity below $I_{res} < 2000 \text{ cts}$. Above this threshold we do not decrease noise but keep it constant (Fig. 14b), indicating that the lowest noise for these certain settings is already reached.

An increased gain influences intensity fluctuations

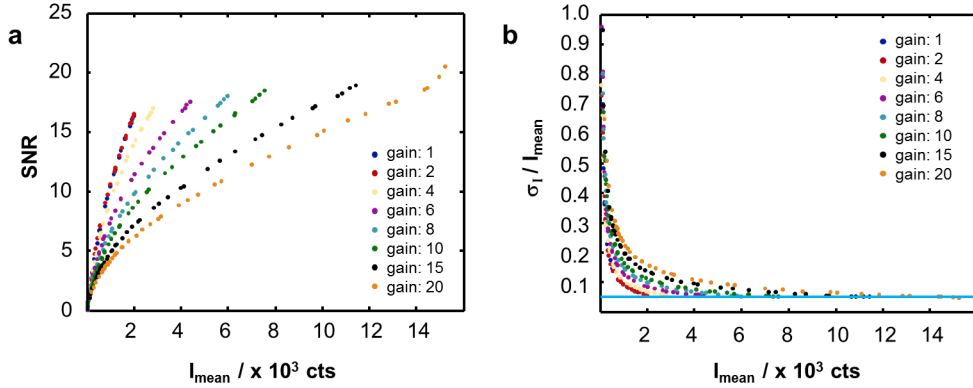


Figure 15: Influence of camera gain settings on intensity fluctuations. a) Increasing the gain decreases the signal to noise ratio (I_{mean}/σ_I). b) Fluctuation in intensity do not decrease to $<5\%$. This threshold is reached at lower intensities with a lower gain.

Looking at the influence of an increased gain on the intensity fluctuations shows that the signal-to-noise ratio here defined as (I_{mean}/σ_I) increases with increasing mean intensities, as expected for shot noise. If we increase the gain of the camera, the relative intensity fluctuations get higher. A SNR of 15 can be already achieved with a mean intensity of 2,000 *cts* at gain 1 but needs a mean intensity of 10,000 *cts* at gain 20 (Fig 15a). With an increasing gain intensity fluctuations increase, but apparently the fitting routine is stable enough to not be effected by these higher intensity fluctuations. Calculating the ratio σ_I/I_{mean} shows that intensity fluctuations do not get better than 5%. With a lower gain we can reach that threshold at lower intensities (Fig 15b).

Setup and measurement procedure was improved mechanically, software-wise and concerning the understanding of noise

To sum up, I was able to implement the correct settings for the camera, especially the crop-mode parameters, in the software, such that they are set automatically at every measurement. The setup has a higher mechanical stability for short time-traces and less noise at higher frequencies, which was mostly achieved by a better local placing of the components and avoiding to use any ventilating system close to the setup, like the camera fan. By improving the focal precision of the refinement procedure, the repeatability of the measurements increased dramatically accompanied by less noise. Background fluctuation of our particles was identified to be dependent on the intensity of the particles and can only be improved with the gain settings of the camera, when we do not exceed a threshold

of 2,000 *cts*. Measurements of events that happen at high frequencies, like diffusion, do not need long measurement times as a certain number of frames is reached faster. As we tend to measure diffusion and weak interactions between particles and our sensors, we stabilized and tuned the setup for the lowest exposure time ($60 \mu s$) and the possible measurement time that can be measured at once with 400,000 frames, before the camera starts a cleaning cycle ($\sim 24 s$). Getting a good understanding on how each setup component and the sensor itself contributes to noise helps in choosing the right sensor and the corresponding settings for a certain measurement.

Silica Coated Gold Nanorods as Dark-field Sensors: A Sensor with Molecular Weight Cut-off and a Mean to Investigate Sensing Distance

Abstract

Silica coated gold nanospheres, and recently also nanorods, are already widely used in sensing mainly because of their high colloidal stability. The mesoporous silica shell surrounding the particles can be synthesized with a defined thickness and also control over pore-size and structure is reported. The silica shell is rigid, stable in water and its thickness can easily be quantified in electron microscopy. For plasmonic sensing building a shell around the nanoparticle surface sounds contradicting, because a part of the sensing volume, in fact the most sensitive part, gets blocked. However, controlling the structure of the shells concerning thickness and porosity opens the door to use these particles as a new type of sensor in single particle dark-field spectroscopy. Here I show that gold nanorods with a defined silica shell can on the one hand be useful to experimentally investigate the effect of a layer around the particle towards plasmon resonance shift $\Delta\lambda_{res}$ in adsorption experiments like NanoSPR, on the other hand enable different functionalization routes (for very thin shells) and find their application as reference particles that are inert to polarizability changes (for very thick shells). Taking advantage of the pore size of the mesoporous shell, I was able to show that these particles are sensors specific for molecules below a certain molecular weight fitting into these pores. This project is still ongoing work but in the following I want to show the proof-of-concept for these sensors for the herein before mentioned applications. The synthesis of the silica coated particles was done with the help of Mathias Schmitt.

Silica coated gold nanorods find widespread application in sensing

Silica coating of gold nanospheres, and later gold nanorods, through a modified Stöber method[37] was already shown a decade ago and found widespread application.[38][39] Nanoparticles coated with silica have an enhanced thermodynamic stability especially when used with pulsed laser in the NIR- or IR-region as done in photoacoustic imaging and photothermal therapy, because the silica shell lowers the interfacial thermal resistance between gold and the surrounding media and prevents nanoparticle melting.[40, 41] Additionally these kind of particles are interesting for imaging in live cells, targeted drug delivery, or any application in biological systems, because of the biocompatibility and the higher stability in biological media of silica compared to an accessible gold surface.[42] Silica coated particles also found a wide application in Surface Enhanced Raman Spectroscopy (SERS) taking advantage of their porosity.[43] The silica shell improves colloidal stability, while the metal surface is still accessible for analytes through the pores, a principle, which is also used for catalysis.[44] Control of shell thickness by the synthetic route is required and well investigated. Furthermore, silica coating opens alternative routes for nanoparticle functionalization: Most functionalization strategies to modify the gold nanoparticle surface are based on strong gold-sulfur interactions, a silica-shell, however, offers hydroxyl-groups on the surface which can be linked to a wide range of functional groups e.g. amines, maleimides and N-hydroxysuccinimides and also facilitates linking to click-chemistry agents.[45]

Taking advantage of silica coating in single particle dark-field spectroscopy

To predict the feasibility of an adsorption experiment (e.g. protein adsorption) on single gold nanorods detected with our dark-field setup, we are interested in the magnitude of the plasmon resonance wavelength shift $\Delta\lambda_{res}$ a single protein adsorption event or a whole layer formation induces on our nanorod. As our sensors are normally coated with a recognition element specific for the analyte, this adsorption is not taking place directly on the nanorod surface, but in a distance dependent on the size of the recognition elements or surface coating. The penetration depth of the induced electric field of the plasmon into the media and with that the sensitivity of our sensors is not infinite, but decays with distance from the nanosensors surface with a decay length d_s , which is a function of the sensors geometry (approximately $d_s = 0.37 \cdot V^{\frac{1}{3}}$). Thus the nanosensor gets less sensitive to adsorption the thicker the layer between an adsorbent and the sensor surface is, as theoretically shown in the previous section. If a shell around the particle has an influence upon the shift of further adsorbed analytes is still an open question and experimental data on single particle level are still missing.

To investigate the effect of layer thickness on shift size experimentally and compare the results with theoretical predictions made in our group, I decided to use silica-coated gold nanorods of different sizes and with different shell thicknesses for adsorption experiments. The advantage of these shells towards layer-by-layer polymer deposition, where the layer thickness can be influenced by the medium, e.g. pH,

salt concentration or temperature, is their rigidity. The thickness of the shell can be determined quite exactly via electron microscopy so that we are able to perform experiments on defined systems. The mesoporous nature of the silica shell can be a disadvantageous for sensitivity measurements, but can also be used to create a sensor, that filters out components of a sample that exceed a certain molecular weight cut-off (MWCO). As a proof of concept for these sensors, I determined the homogeneity of the layer thickness, which results to be defined enough to perform sensitivity measurements. I was able to obtain shells that shield the entire sensing volume of the nanorods and who are indeed able to selectively sense smaller molecules through their pores and filter out bigger proteins. These sensors can also be used as reference particles for single wavelength measurements, which will be also shown in this section.

Silica shells are homogeneous with an ensemble standard deviation of around 10%

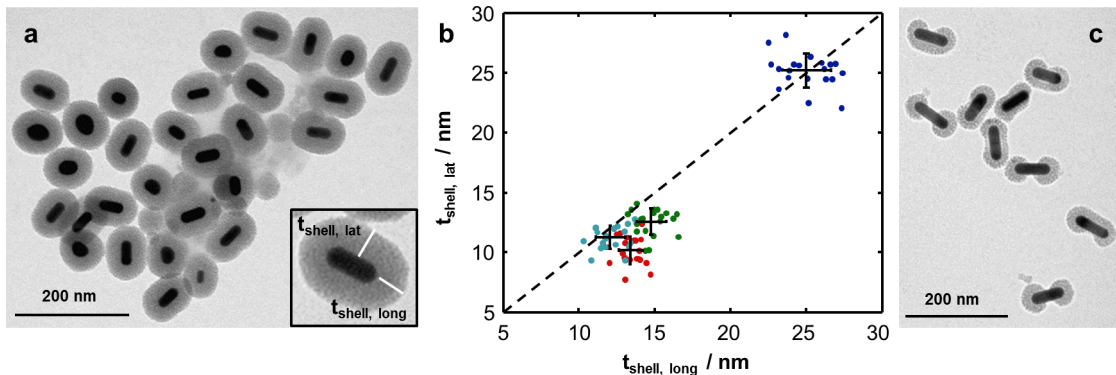


Figure 16: Evaluation of the silica shell homogeneity. a) TEM-image of silica coated gold nanorods. Particles without coating were not observed. The shell thickness was evaluated for the longitudinal axis ($t_{shell, long}$) and the transversal axis ($t_{shell, lat}$) independently. b) Correlating the two axis for four different silica coated particle samples (each color indicates one sample) shows that for particles with a shell thickness $t_{shell} < 20 \text{ nm}$ the longitudinal axis is slightly longer, with a ratio $t_{shell, long}/t_{shell, lat}$ of 1.07 (turquoise), 1.17 (green) and 1.32 (red) and are more uniform with $t_{shell, long}/t_{shell, lat} = 0.99$ for particles with bigger shells (blue). This thickness distribution is not dependent on gold nanorod size as two types of particles were coated: Type A with a width of $w = (16.78 \pm 1.23) \text{ nm}$ and a length of $l = (45.28 \pm 3.33) \text{ nm}$ (blue and green) and type B with a width of $w = (19.44 \pm 3.67) \text{ nm}$ and a length of $l = (59.19 \pm 7.37) \text{ nm}$ (turquoise and red). In general the standard deviation of the size is around 10%. c) In some samples it was observed that coating can be restricted to the tips, which is interesting for the investigation of the local sensitivity distribution amongst the rod surface.

Generally, silica coating is done by a modified Stöber-method. In the case of nanorods CTAB localized on the particles surface can serve as organic template for silica formation. The silica precursor tetraethylen orthosilicate (TEOS) is reported to hydrolyze and subsequently condensate on the surface of the CTAB molecules at a basic pH.[39] The control of silica shell thickness during synthesis can be done by two different ways. On one hand control can be achieved by the amount of TEOS and the reaction time at a constant CTAB concentration[46] and on the other hand by adjusting the concentration of CTAB in the reaction tube.[47] Very thin shells of around 2 nm can be obtained by quenching the reaction with poly(ethylene glycol) silane (PEG-silane).[46]

Determination of the shell thickness of silica over-coating and its homogeneity in size via electron microscopy showed at first, that the coating is homogenous regarding the whole sample. The shell thickness shows a standard deviation of around 10% in size and no uncoated particles were found in the TEM-images (Fig. 16a and b). Evaluating single particle shell homogeneity regarding their growth in length ($t_{shell, long}$) and width ($t_{shell, lat}$), exhibits that the shell is slightly thicker in length than in width for $t_{shell} < 20\text{ nm}$, but with a ratio of $t_{shell, long}/t_{shell, lat} < 1.3$ and gets more homogenous for thicker shells (Fig. 16b). In some occasions we could observe that incomplete layer formation at certain reaction conditions leads to silica coating restricted to the tips of the nanorods (Fig. 16c). As the electric field enhancement is highest at the tips of the nanorods, the sensitivity to an analyte is highest at these points as well. Blocking the tips by silica coating can give an experimental insight into the influence of the tips to sensor sensitivity. Herein, the plasmon resonance shift by changing the refractive index of the surrounding media should decrease dramatically. Because of the shown sample homogeneity of the silica shells, they are suitable tools for investigating layer effects on resonance shift upon adsorption on these passivating layers. Further because of the rigidity of the shell and the possibility for quantification in electron microscopy, one can track the particles via a TEM finder grid directly after measurement in the dark-field microscope and determine the shell thickness of exactly the same particles.[48]

Pore volume of silica shells can be estimated from sensitivity measurements

The sensitivity S of a nanoparticle is defined as the plasmon resonance wavelength shift upon changes in refractive index n , $S = \frac{\Delta\lambda_{res}}{\Delta n}$, and is a parameter that is highly dependent on the aspect ratio of the nanorod $S = 114 \cdot AR$. To measure the sensitivity of a nanoparticle sample we change the medium in the flow-cell from water to a medium with a higher refractive index, e.g. water/glycerol mixtures. By this procedure, we can make sure, that the whole sensing volume V_{sens} of the particle is filled with the same medium and the obtained shift is the maximum shift that we can get for the medium of a certain refractive index. If we block a part of the sensing volume of a particle the sensitivity does not change, but the shift $\Delta\lambda_{res}$ is reduced by a factor dependent on the accessible volume V_{free} , $\Delta\lambda_{res} = S \cdot \Delta n \cdot \frac{V_{free}}{V_{sens}}$ under the assumption that the sensitivity is constant over the whole sensing

volume. In fact the sensitivity is distance dependent from the nanorod surface (see equation 6). The sensing volume is reduced when a particle is lying on the surface of a flow cell, because its bottom part is not longer accessible, but can be also reduced by a silica shell.

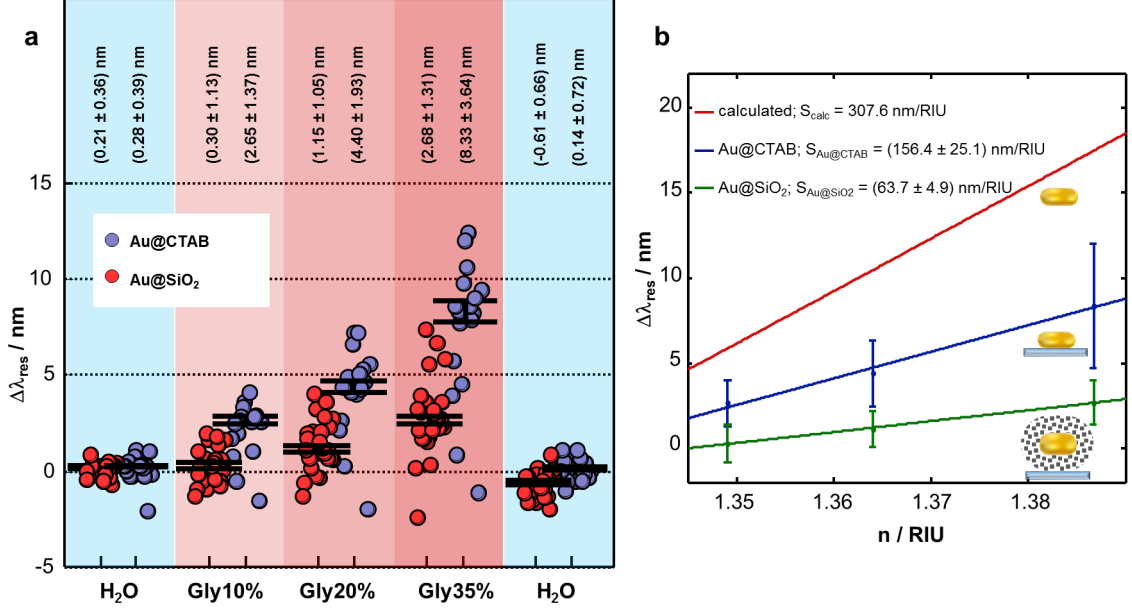


Figure 17: Sensitivity measurements with silica coated gold nanorods. a) Silica coated gold nanorods, Au@SiO₂, (red) and bare CTAB gold nanorods, Au@CTAB, (blue) were incubated subsequently with media with increasing refractive indices and their plasmon resonance wavelength shift $\Delta\lambda_{res}$ was recorded. b) Fitting $\Delta\lambda_{res}$ gives a smaller sensitivity $S_{Au@CTAB} = (156.4 \pm 25.1) \text{ nm}/RIU$ for CTAB-rods (blue) compared to the calculated sensitivity $S_{calc} = 307.6 \text{ nm}/RIU$ (red), because of partially shielding of the sensing volume by the glass surface of the flow cell. The even smaller sensitivity for the silica coated nanorods of $S_{Au@SiO_2} = (63.7 \pm 4.9) \text{ nm}/RIU$ (green) can be explained by the volume of the pores.

Measuring the $\Delta\lambda_{res}$ for silica coated gold nanorods with a shell thickness of $t_{shell} = (24.97 \pm 2.96) \text{ nm}$ and the bare particles from the same batch with a width of $w = (16.78 \pm 1.23) \text{ nm}$ and a length of $l = (45.28 \pm 3.33) \text{ nm}$ in different media with increasing refractive index (10% glycerol in water: $n = 1.349$; 20% glycerol in water: $n = 1.360$; 35% glycerol in water: $n = 1.387$), we can observe that the silica coated particles shift less than the bare particles, as expected (Fig 17a). Fitting $\Delta\lambda_{res}$ we obtain a sensitivity for the silica coated gold nanorods $S_{Au@SiO_2} = (63.7 \pm 4.9) \text{ nm}/RIU$ that is much lower than for the bare particles with a sensitivity of $S_{Au@CTAB} = (156 \pm 25.1) \text{ nm}/RIU$ (Fig 17b). Considering the theoretically calculated sensitivity for these particles $S_{calc} = 307.6 \text{ nm}/RIU$ and the fact that the sensitivity is an intrinsic property of the particle and does not change, we can calculate the

accessible volume fraction $V_{frac} = \frac{V_{free}}{V_{sens}}$ by $V_{frac} = \frac{S_{meas}}{S_{calc}}$ for the two types of particles, respectively. For the bare rods lying on the flow-cell surface 50% of the volume is accessible, for the silica coated gold nanorods 20% of the sensing volume is accessible. The calculated sensing distance of these nanorods is $d_s = 7.63 \text{ nm}$. Thus with a shell thickness of $t_{shell} = 24.97 \text{ nm} > 3 \cdot d_s$ these particles should, following equation (6), not respond with a shift $\Delta\lambda > 0.02 \text{ nm}$ to a refractive index of $\Delta n_{35\%Gly} = 0.06$ in their surrounding, but as the shell is porous it happens that the small glycerol molecules can come close to the particle and induce a shift. The calculated 20% of accessible volume ergo refers to the volume of the pores, as the flow-cell surface should have less influence (see inlets in Fig. 17b). Taking advantage of this behavior for sensing, we can create a sensor, that lets analytes fitting in the pores pass for detection, while bigger components of the sample are filtered out.

Blocking of sensing distance for analytes with a certain molecular weight cut-off

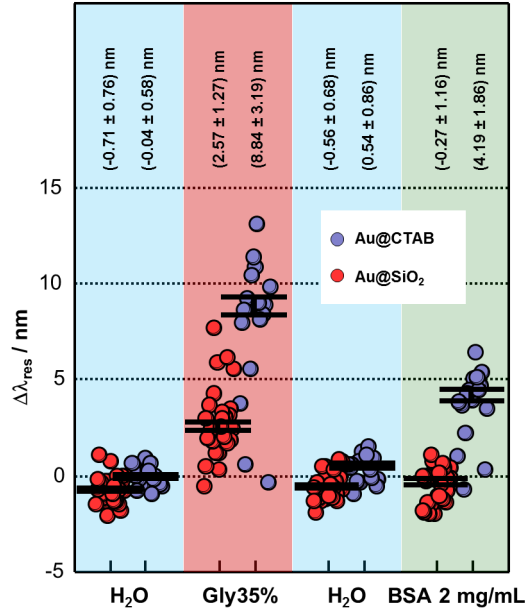


Figure 18: Silica coated gold nanorods as sensors with a molecular weight cut-off are only sensitive to smaller molecules. Silica coated particles (Au@SiO_2 , red) and bare particles from the same batch (Au@CTAB , blue) were first incubated with 35% glycerol in water, which gave a reversible shift of $\Delta\lambda_{res, \text{Au@CTAB}} = 8.84 \text{ nm}$ for the CTAB particles and a smaller shift of $\Delta\lambda_{res, \text{Au@SiO}_2} = 2.57 \text{ nm}$ for the silica coated particles. Because of its small molecular size glycerol can enter in the pores of the silica shell. Incubating the particles with BSA the CTAB particles shifted $\Delta\lambda_{res, \text{Au@CTAB}} = 4.19 \text{ nm}$ while the pore sizes of the silica shells are too small to let BSA enter and be sensed.

For many sensing applications, we do not have exclusively one analyte in the sample that has to be probed, but several.[30] For detection of certain molecules in biological samples, for example in blood serum, it would be advantageous to exclude a part of the proteins from entering the sensing volume and from getting close to the recognition elements on the sensor surface. Silica is known to be mesoporous with pore sizes of about $2 - 30 \text{ nm}$. [49] The pore size is reported to be controllable by interconnected parameters, i.e. the length of the surfactant chain on the particle, the solvent, stirring speed and reaction temperature. Also the arrangement of the pores (radial, parallel or disordered) can be influenced.[50] Using silica coated particles as sensors, the pore size can determine the molecular weight cut-off of the molecules, that can enter the pores and come close enough to the metal surface to influence the electric near-field of the plasmon and be detected. To prove this principle for our measurements, we used a quite drastic size difference of analytes. On the one hand BSA, that has a molecular weight of $MW = 66 \text{ kDa}$, which corresponds to a diameter of $\sim 4 \text{ nm}$, and on the other hand glycerol in water that is a small molecule. Immobilizing silica coated gold nanorods and bare nanorods from the same batch on a flow-cell surface and changing the surrounding media from water to glycerol demonstrates that the silica coated particles are still sensitive to the refractive index change induced by glycerol, but in a less extend than the bare rods, as explained in the previous section. Incubating the particles with BSA shows that the size of this protein is too big to enter the pores and therefore no shift can be observed in contrast to a shift of $\Delta\lambda_{res} = (4.19 \pm 1.86) \text{ nm}$ for the CTAB particles where the BSA covers the gold nanorod surface (Fig. 18). A sensor particle that is totally inert against adsorption of proteins exceeding a certain molecular weight cut off can also find their application as reference particles.

Silica-coated particles can be used as reference particles for single wavelength measurements

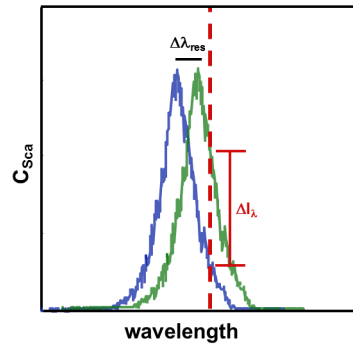


Figure 19: Sensing principle for single wavelength measurements. A shift in plasmon resonance wavelength goes along with a change in intensity $I \propto C_{sca}$ when measured at a single wavelength.

Plasmon shifts caused by refractive index changes also induce changes in the wavelength dependent scattering cross section of a particle illuminated with a single wavelength (see equation 1). Since $I \propto C_{Sca}$ a plasmon shift can be detected as an intensity change ΔI_λ (Fig. 19).[31] The advantage is that the scattering intensity of thousands of particles can be detected at once on a camera chip. The complication lies in the precision and stability of the measurements: a small focal change or some background scattering from the surface or the medium can be disturbing and falsify the measurement. Correction for these artifacts can be done by reference particles. These particles are supposed to be inert against adsorption of a protein e.g. because of their surface functionalization, for example methoxy-(polyethylene glycol) particles. Although the binding affinity of proteins to this coating is low, adsorption could still take place. Apart of the surface functionalization, it is also possible to use particles, which are modified that way, that analytes can simply not get so close to the sensors, that they induce a plasmon shift, as it is the case for silica coated gold nanorods, whose silica shell thickness t_{shell} exceeds the sensing distance of the particle $t_{shell} \gg d_s$.

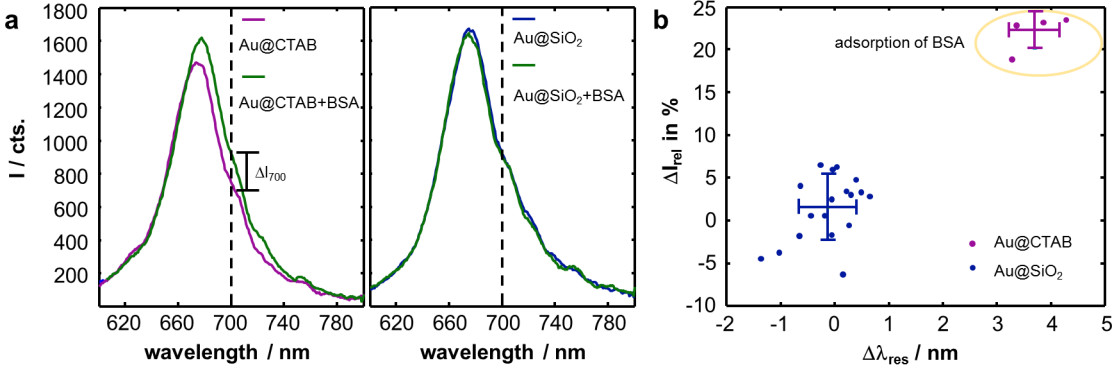


Figure 20: Silica coated gold nanorods as reference particles in single wavelength measurements. a) Changes in single particle spectra upon BSA adsorption. While on bare particles (Au@CTAB) BSA adsorption induces a shift in resonance wavelength $\Delta\lambda_{res}$ as well as an increase in intensity ΔI_{700} at a wavelength of $\lambda = 700\text{ nm}$ (left), the silica coated particles Au@SiO₂ are inert to refractive index changes in their surrounding (right). b) Correlation of relative intensity change ΔI_{rel} at $\lambda = 700\text{ nm}$ to $\Delta\lambda_{res}$ for Au@CTAB (magenta) and Au@SiO₂(blue) indicates that silica coated gold nanorods are inert and do not shift neither in resonance wavelength $\Delta\lambda_{res, Au@SiO_2} = (-0.12 \pm 0.54)\text{ nm}$ nor significantly in intensity $\Delta I_{rel, 700\text{ nm}} = 1.43\% \pm 3.83\%$, whereas bare particles show the expected behavior of a plasmon resonance wavelength shift of $\Delta\lambda_{res, Au@CTAB} = (3.70 \pm 0.47)\text{ nm}$ and a relative increase in intensity of $\Delta I_{rel, 700\text{ nm}} = 22.14\% \pm 2.16\%$.

Using gold nanorods with a width of $w = (16.78 \pm 1.23)\text{ nm}$ and a length of $l = (45.28 \pm 3.33)\text{ nm}$, their sensing distance amounts to $d_s = 7.63\text{ nm}$. Thus, with a silica-shell of $t_{shell} = (24.97 \pm 2.96)\text{ nm}$ we cover more than 95% of the sensing volume and do not observe a shift upon adsorption neither

in resonance wavelength, nor in intensity, in contrast to bare particles after incubation with *bovine serum albumine* (BSA) (Fig. 20a). A shift in plasmon resonance wavelength, caused by adsorption of BSA on bare particles, of $\Delta\lambda_{res, Au@CTAB} = (3.70 \pm 0.47) nm$ induces a significant relative intensity change of $\Delta I_{rel, 700nm} = 22.14\% \pm 2.16\%$. The intensity change of the silica coated particles is $\Delta I_{rel, 700nm} = 1.43\% \pm 3.83\%$ if no plasmon resonance wavelength shift was detected (Fig. 20b). Intensity fluctuations of 5% satisfy with the standard deviation of intensity fluctuations observed when measuring time traces and can be considered as not significant (see Fig. 15b). For this comparison particles were chosen, that have similar resonance wavelength positions so that an intensity change at a certain wavelength should correspond to a similar plasmon resonance wavelength shift. These results demonstrate that by using silica-coated gold nanorods as reference particles to measure a plasmon shift as a shift in scattering intensity at a fixed wavelength, we can justify if we detect a plasmon shift or intensity changes by outer influences.

Proof-of-principle for silica coated nanorods as sensors in dark-field microscopy

Although it is thought to be contradicting to cover the most sensitive part of a sensor surface with a shell, I want to avail on this procedure to get a better understanding on sensing. Building well defined, homogenous and quantifiable shells around a nanorod and test their influence on the plasmon resonance wavelength induced by protein adsorption can validate our theoretical calculation of the sensing distance and also elucidate the effect of a passive layer upon the same. Performing these measurements is still required and I showed that the silica shells are homogeneous enough to be used as sensors for these experiments. Further, I proved that these particles can be used as reference particles in single-line measurements, since their plasmon does not shift upon presence of a protein, when the shell thickness is big enough to shield the entire sensing volume and the protein is not able to enter the pores. The use of plasmonic reference particles can help a lot in identifying artifacts in these kind of measurements. A totally new field on plasmon sensing with dark-field microscopes would be to use silica coated particles as molecular weight cut off sensors, as I tried it successfully for glycerol and BSA. While glycerol can enter the pores, BSA can not be sensed as it can not come close enough to the sensor surface. Especially for multiplexed measurements in crowded biological samples, like blood serum, this approach would be a big advantage. For further investigation synthesizing silica shells with radial pores would be a prosperous next step.

NanoSPR for Oligomer-Forming Proteins: Investigating the Adsorbed Species and Its Binding Affinity Simultaneously

Abstract

Recently we demonstrated that we are able to perform measurements to characterize binding affinities of protein-protein interactions on single plasmonic nanosensors with our dark-field microscope.[33] In principle one protein is immobilized on a plasmonic nanosensor and the adsorption of a protein interacting with the immobilized one can be measured as a refractive index change in the near environment of the nanosensor shifting its plasmon resonance wavelength, similar to surface plasmon resonance spectroscopy (SPR). The extent of the plasmon resonance shift is dependent on the number of adsorbed proteins, i.e. the analyte concentration and its binding affinity. If analyte concentration is low enough to resolve single analyte adsorption the plasmon resonance wavelength shift reflects the size of the analyte.[34] In nature a lot of proteins exist, that form higher ordered oligomeric structures. For some of them the oligomeric structure is the reactive species, for others it is a storage form and protomers can be released if needed. As we are able to predict the plasmon resonance wavelength shift a defined structure induces upon adsorption on our nanosensors, we can identify the reactive species (protomers or oligomers) interacting with our nanorods during an adsorption experiment. One of these proteins is IM30, a protein that forms oligomeric ring structures of 12-17 subunits and that is known to adsorb on negatively charged lipids. Here I show that we can determine its binding affinity in a simple NanoSPR experiment and that we are able to simultaneously identify the adsorbed species for this protein, which is not the ring structure, without the need to measure with high time resolution. With these experiments I was able to contribute to the understanding of the behavior of an important protein. This project was carried out in collaboration with the group of Prof. Dr. Dirk Schneider (Institute of Biochemistry, Mainz) who provided the protein and is published in [51].

Adsorption on small sensors

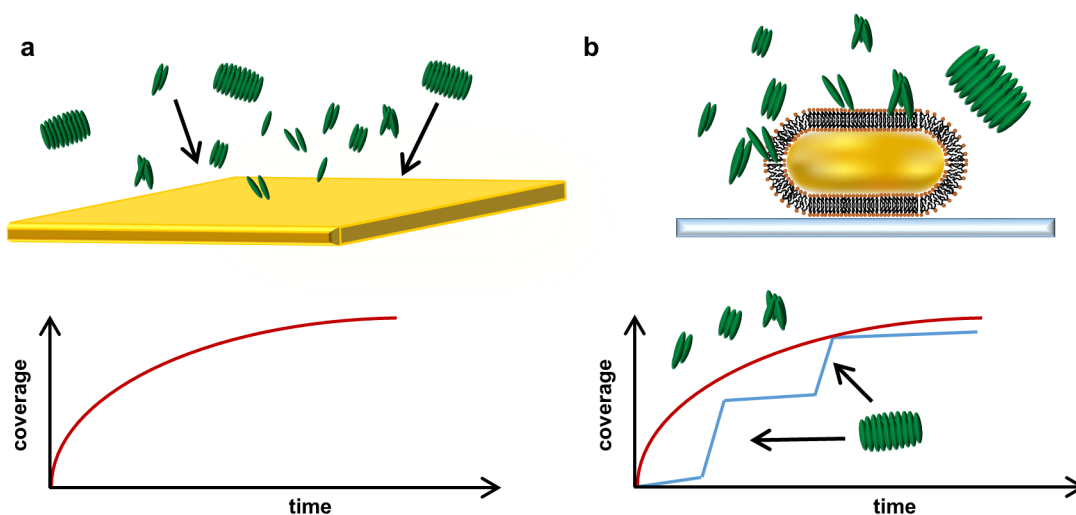


Figure 21: Difference in protein adsorption behavior on big sensors (SPR) and on nanosensors. a) On a SPR chip whose size is 1 cm^2 we see a smooth increase in coverage over time, as the response to a single protein is too small to be resolved and we have many adsorption steps. b) Adsorption on a nanosensor shows the same behavior for very small proteins. For bigger proteins, where only a hand full can fit on the sensor, we can see a defined number of adsorption steps. The response of the sensor towards adsorption of a single protein is much higher and can be quantified.

Nanorods for plasmon sensing have a size of around $20 - 50\text{ nm}$ in width and $50 - 100\text{ nm}$ in length. Being in this nanometer range the sensors approach the size of the proteins, that are supposed to adsorb upon them. For a fixed sensor size, this means the bigger the analyte, the less of them can adsorb on the sensor surface and their number can be calculated. Further the shift of the plasmon resonance wavelength of the nanosensor is higher the bigger the analyte. The shift size per protein can be theoretically calculated and quantified during an adsorption measurement. If a mixture of proteins with different sizes adsorbs upon a sensor for surface plasmon resonance spectroscopy (SPR), whose size is normally 1 cm^2 , we will result in a smooth coverage increase over time, independently on the size of the adsorbed protein species, small protomers or bigger oligomers (Fig. 21a). Conducting the same experiment on a nanosensor makes it possible to identify adsorption of bigger analytes in the extent of the plasmon resonance shifts and a reduced number of bigger proteins that fit on a surface can also be identified as less adsorption events (Fig. 21b). Thus it is possible to determine the defined species in a mixture of proteins that have different sizes, as it is the case for oligomer forming proteins.

IM30 (Vipp1) – a very important protein in plastids

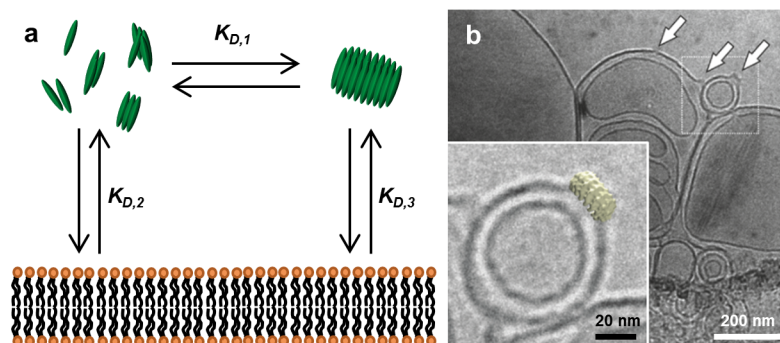


Figure 22: IM30 is an oligomer-forming protein, that forms ring structures and adsorb on negatively charged lipids. a) IM30 forms oligomers up to ring structures. Whether ring-formation is prerequisite to adsorb on lipid bilayers or also lower ordered oligomers are able to adsorb is questioned. b) The adsorption of ring structured IM30 could be observed in electron microscopy. Smaller structures of the protein would escape analysis, because of their small size. Picture taken from [52]

The *internal membrane-associated protein of 30 kDa* (IM30) formerly known as *vesicle inducing protein in plastids 1* (Vipp1) is an oligomer forming protein which is involved in the biogenesis and maintenance of thylakoid membranes in chloroplasts and cyanobacteria.[53] IM30 is able to form dimers and out of these high-ordered oligomeric ring structures, where the ring members vary between 12-17 dimers, resulting in a molecular mass of the rings between 1.6 – 2.2 *MDa* and diameters between 25 – 33 *nm*. [54] So far, only little is known about the function of this protein especially with regard of the need to build oligomeric structures. The absence of IM30 results in a decreased amount of thylakoid membranes and as a consequence from this to less photosynthetic activity of a plant, which explains the importance of this protein.[55] Recently, IM30 was shown to be able to reorganize lipid structures and initialize membrane fusion in chloroplasts.[52] The interactions between IM30 and membranes occurs specifically with lipids having negatively charged head-groups such as phosphatidylglycerols, that are highly abundant in thylakoid membranes. Because of the fact that IM30 does not assemble in a single ring species, but in rings with a varying amount of IM30 subunits it seems unlikely, that the ring structure is the active form. Although IM30 rings were observed to interact with membranes in electron microscopy,[52] it is likely that the monomers or smaller ordered oligomers can escape observation due to their small size.

To gain insight into the thermodynamics of the interactions between negatively charged lipids and IM30 we use lipid coated plasmonic gold nanorods as sensors and perform NanoSPR measurements, where we measure the plasmon resonance wavelength shift of single nanosensors during the adsorption process in a dark-field spectroscopy setup.[33] Evaluating the plasmon resonance shifts during the

adsorption process and comparing their size to a theoretically expected shift calculated for the ring structure exhibits that the measured shifts are smaller. Hence we can conclude that ring formation is not prerequisite for adsorption. Thus, from the plasmon resonance wavelength in equilibrium for different protein concentrations we obtain the dissociation constant of lower-ordered oligomers.

Lipid coated gold-nanorods as sensors have advantages to supported lipid bilayers

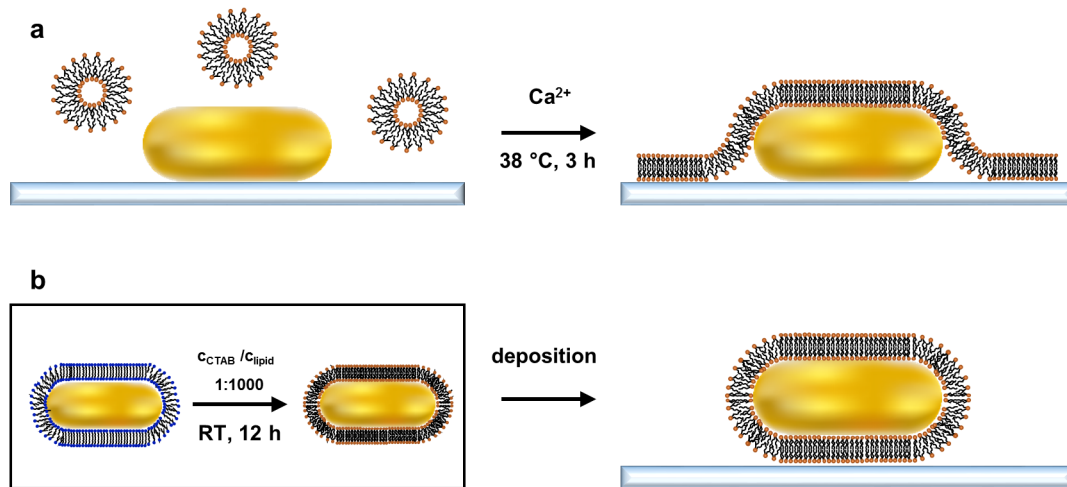


Figure 23: Strategies to obtain lipid bilayer covered nanosensors. a) The nanorods are deposited on the glass flow-cell surface and a supported lipid bilayer is spread over the whole glass surface including the nanorods. b) In a pre-coating step the particles are incubated in a reaction tube with a high excess of lipids compared to the CTAB concentration stabilizing the nanorods on the surface. CTAB gets exchanged by the lipids. After coating, the particles can be deposited on the flow-cell surface.

To measure protein interaction with a lipid bilayer we routinely spread a supported lipid bilayer (SLB) on top of the whole flow-cell surface including the immobilized gold nanosensors (Fig. 23a).[56][57] A successful formation of a lipid bilayer of the negatively charged dioleoylphosphatidylglycerol (DOPG) in the flow-cell could be performed, but under harsh conditions: heating, high Ca^{2+} concentration and a long incubation time, which makes this procedure very time-consuming. As we do not want to measure dynamics over a big area, like for example for the Min-dynamics,[57] we only require the sensor itself to be covered by the lipid bilayer. Thus the nanorods were pre-coated with lipids before

they were deposited on the flow-cell surface (Fig. 23b). This procedure has the advantage, that we perform a one time coating of a stock of particles, which we can use over the time. Except of being less time- and material-consuming, this procedure has the advantage, that all sensors that we use for our experiments suffer the same treatment and react in the same way.

Lipid coated particles are highly stable and sensitive to IM30

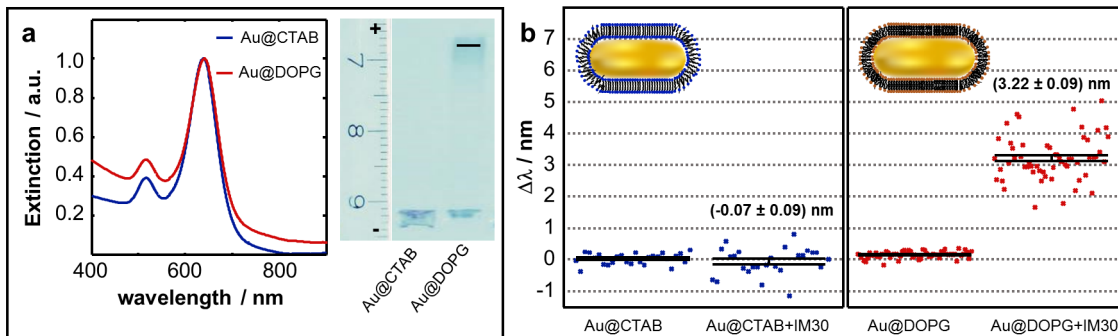


Figure 24: Functionalization is successful and lipid coated particles are sensitive to IM30. a) Extinction spectra of Au@CTAB ($\lambda_{res} = 638$ nm, blue) and Au@DOPG ($\lambda_{res} = 640$ nm, red) show a shift in plasmon resonance of 2 nm and do not exhibit particle aggregation during functionalization. In gel electrophoresis Au@CTAB aggregate in the well of the gel, while Au@DOPG migrate because of their negative charge. b) Adsorption of IM30 ($c = 0.4$ μ M) on Au@CTAB and Au@DOPG prove the adsorption of IM30 on Au@DOPG with a shift of $\Delta\lambda_{res} = (3.22 \pm 0.09)$ nm, while no adsorption is observed on Au@CTAB.

Lipid coating of nanoparticles was already reported for zwitterionic phosphocholine lipids, but not for negatively charged ones as in the case of DOPG.[58] For the surfactant exchange from CTAB to DOPG the particles are incubated with a high excess of lipids. A successful functionalization of gold nanorods with DOPG was verified via UV-vis spectroscopy and gel electrophoresis. By changing the particle surrounding, the plasmon resonance wavelength of the nanorods changes slightly and aggregation of particles caused by instability can be observed in a peak rising at a wavelength range between 800 – 900 nm. UV-vis extinction spectra show a red shift of the plasmon resonance wavelength for the lipid coated particles (Au@DOPG) of 2 nm and do not exhibit particle aggregation. (Fig. 24a, left). In gel electrophoresis a change in the mobility of the particles in the gel can be observed. CTAB gold nanorods (Au@CTAB) aggregate in presence of the working buffer, while for Au@DOPG we expect them to have a high mobility because of their negative charge. Comparing the mobility of functionalized (Au@DOPG) and unfunctionalized (Au@CTAB) particles in gel-electrophoresis, Au@DOPG show the expected behavior (Fig. 24a, right). The stability of the particles in the working buffer (Hepes 20 mM,

pH 7.6) was also proven: after three days in this buffer the particles did not aggregate and showed the same gel-mobility as before (see appendix). The sensitivity of Au@DOPG towards IM30 was tested by incubating Au@CTAB and Au@DOPG with the same concentration of IM30. While the Au@DOPG show a shift of $\Delta\lambda_{res} = (3.22 \pm 0.09) nm$ due to protein adsorption, the plasmon resonance wavelength of Au@CTAB does not shift (Fig. 24b).

The shift-sizes of an IM30 ring-structure can be calculated

The plasmon resonance wavelength λ_{res} of gold nanorods shifts due to changes in the polarizability or refractive index (Δn) in the immediate environment. Polarizability can change due to the formation of a dense layer around the particle or even due to binding of a single protein. We can calculate the shift of the plasmon resonance wavelength induced by the binding of a single IM30 ring $\Delta\lambda_{ring}$ in order to compare this shift with those shifts measured over time in experiments to estimate the presence or absence of ring-binding events. The plasmon resonance shift $\Delta\lambda_{res}$ is proportional to the amount of refractive index change Δn with a proportionality constant or sensitivity S . Furthermore, the magnitude of the plasmon resonance shift $\Delta\lambda_{res}$ decreases exponentially with increasing distance from the sensor surface with a characteristic distance or sensing distance d_s . Both S and d_s are functions only of the gold nanorod's geometry (length and width) and either measured or estimated theoretically by numerically solving Maxwells equations (using tabulated dielectric constants). In our case, we use $S = (143.1 \pm 39.5) nm/RIU$ (measured) and $d_s = (14.3 \pm 2.6) nm$ (calculated). Knowing S and d_s , the resonance wavelength shift for a protein layer $\Delta\lambda_{layer}$ with thickness t protein is given by:

$$\Delta\lambda_{layer} = S\Delta n (1 - e^{-\frac{t_{protein}}{d_s}}) \quad (9)$$

In our case, the proteins are not adsorbing directly on the particle surface but on a lipid bilayer (with thickness $t_{bilayer} = 5 nm$) surrounding it. The increased distance to the nanoparticle surface has to be taken into account by subtracting the shift produced by the lipid bilayer from the total shift of the bilayer and the protein. The resulting plasmon resonance wavelength shift $\Delta\lambda_{layer}$ of a complete and dense layer of IM30 is then:

$$\Delta\lambda_{layer} = S\Delta n [(1 - e^{-\frac{t_{protein}+t_{bilayer}}{d_s}}) - (1 - e^{-\frac{t_{bilayer}}{d_s}})] \quad (10)$$

The plasmon shift induced by a single IM30 ring ($\Delta\lambda_{ring}$) follows by dividing by the number N_{rings} of IM30 rings than that would fit into the volume of a complete protein layer around the particle, which we estimate by the relative volumes $N_{protein} = V_{layer}/V_{ring}$. Using the known particle dimensions, the bilayer thickness and the IM30 ring dimensions reported in [54] (25 – 33 nm in diameter, 22 nm in height), we estimate a maximum of 23-40 rings per nanoparticle, dependent on the ring diameter. Using the standard assumption for the refractive index for biomolecules of $n = 1.5$, [59] i.e. $\Delta n = 0.17$, we

arrive at a resonance wavelength shift for the binding of a single IM30 ring of $\Delta\lambda_{ring} = 0.47 - 0.82 \text{ nm}$, dependent on the diameter of the ring.

To determine the amount of potential IM30 ring binding events, we evaluate the shifts in the resonance wavelength position between two consecutive measuring points $\Delta\lambda_i$ for each individual particle until 90% of the resonance wavelength shift in equilibrium ($\Delta\lambda_{eq}$) was reached. Only when the determined $\Delta\lambda_i$ between two measuring points exceeded the calculated level of $\Delta\lambda_{ring}$, the determined $\Delta\lambda_i$ could possibly be caused by binding of an IM30 ring to the membrane covered gold nanorod. However, it is worth mentioning that a measured $\Delta\lambda_i \geq \Delta\lambda_{ring}$ could also be caused by consecutive binding of multiple lower-ordered IM30 oligomers or even monomers that occurred faster than the time resolution of the measurement. As in the sample we have a variation of ring sizes, we calculated the shifts $\Delta\lambda_i \geq \Delta\lambda_{ring}$ for the smallest rings (25 nm in diameter) and the biggest rings (33 nm in diameter) separately to obtain borders where the sample behavior should lay in between.

Since we are approaching the protein size with the size of our sensor we can additionally calculate the number of IM30 rings that can fit spatially on the sensor surface. Our sensor lies on a flow-cell surface, which shields around one third of the bottom part of the sensor surface and we assumed 60% of the sensor surface area to be available for adsorption. Furthermore, proteins on the surface are not densely packed, but absorb up to an available surface coverage limit of around 55%. [60] If we calculate the number of IM30 rings, whose diameter vary between 25 – 33 nm that can than absorb on top of a single gold nanorod we end up with a number of 4-7 rings, dependent on the number of protomers per IM30 ring. The values are calculated from the footprint of the IM30-ring on the particle surface area. The geometry of the nanorod is described to be a cylinder with spherical shaped caps. The dimensions are given by the dimensions of the nanorod itself with a 5 nm lipid bilayer on top.

Adsorption behavior of the protein gives insight in adsorbed species

To quantify the adsorption behavior of IM30 on Au@DOPG we incubate the particles with increasing concentration of IM30 and detect the resonance wavelength shift over time. The protein is flushed into the flow-cell and the plasmon resonance wavelength shift $\Delta\lambda_{res}$ of every sensor particle was recorded every 60 – 90 s. According to our calculations, for an adsorption of exclusively IM30 rings, we would expect an adsorption curve that consists of not more than 4-7 discrete steps of at least 0.47 nm height, the shift the smallest IM30 ring induces adsorbing on the nanosensors. However we obtain adsorption curves for adsorption on single particles, on the averaged curves these steps can average out, that look relatively smooth and do not exhibit such steps (Fig. 25a). To quantify this observation, we calculate the percentage of $\Delta\lambda_i$ between two measuring points that exceed the shift we estimated for the ring binding ($\Delta\lambda_{ring}$) for each measured IM30 concentration. These percentages are calculated for a binding of exclusively small rings of 25 nm in diameter ($\Delta\lambda_{ring} = 0.47 \text{ nm}$; turquoise data points in Fig. 25b) and exclusively big rings of 33 nm in diameter ($\Delta\lambda_{ring} = 0.82 \text{ nm}$; yellow data points

in Fig. 25b). Since we have a distribution of ring sizes in the sample the percentage of shifts that can be caused by ring binding in our measurements lies somewhere between those calculated borders (blue-white crossed areas in Fig. 25b). The number of shifts that exceed the theoretically calculated threshold for adsorption of a single ring also if only the smallest rings would bind was usually below 25% (with an outlier for $c_{IM30} = 1.58 \mu M$).

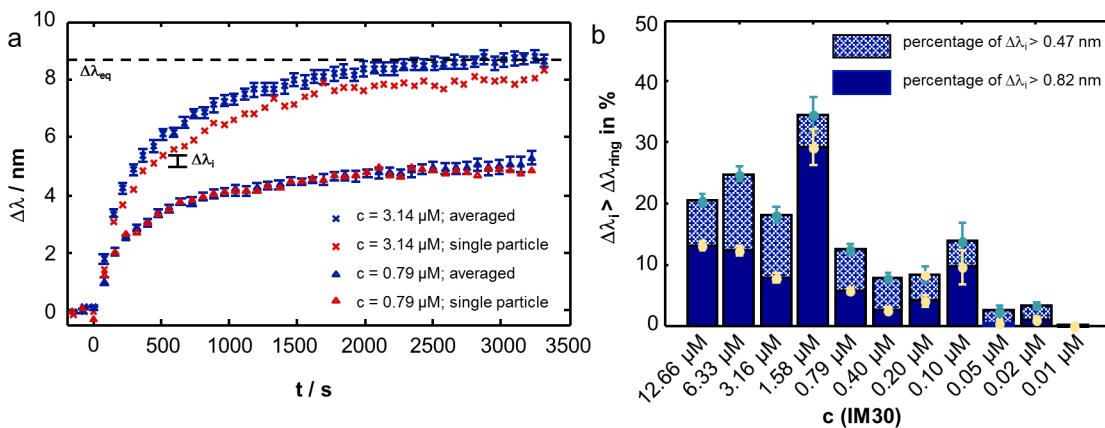


Figure 25: Quantification of the shift size during adsorption. a) Two adsorption curves for different protein concentrations (crosses: $c_{IM30} = 3.14 \mu M$; triangles: $c_{IM30} = 0.79 \mu M$) as example. Blue curves show the average over around 20 particles, red curves show single particle data. $\Delta\lambda_i$ is the shift between two measured time steps. $\Delta\lambda_{eq}$ is the resonance wavelength shift in equilibrium and is used to determine the dissociation constant. b) Calculated percentages of shift sizes that exceed the threshold of $\Delta\lambda_{ring} = 0.47 nm$ for small rings with $25 nm$ in diameter (blue-white crossed bars, turquoise dots show data points and standard error) and percentages of shift that exceed the threshold of $\Delta\lambda_{ring} = 0.82 nm$ for big rings with $33 nm$ in diameter (blue bars, yellow dots show data points and standard error) for each concentration respectively. The data points show are calculated borders. As we have a distribution of ring sizes in the sample the percentage of shifts caused by ring adsorption lies somewhere in the blue-white crossed areas that are not covered. The percentage of $\Delta\lambda_i$ that exceeds $\Delta\lambda_{ring}$ is usually below 25% and is higher for higher IM30 concentrations, since more proteins adsorb between a certain time-step.

The concentration dependency is due to the fact that at higher concentrations a consecutive binding of many proteins can take place and is faster than the time resolution of the measurements. These results show that IM30 binds predominantly as smaller oligomers than as high ordered rings to our Au@DOPG particles and a dissociation constant obtained by measurements with NanoSPR therefore reflects the dissociation constant of lower ordered oligomers or even single protomers.

Thermodynamic dissociation constant K_D of IM30 and PG-bilayers was measured

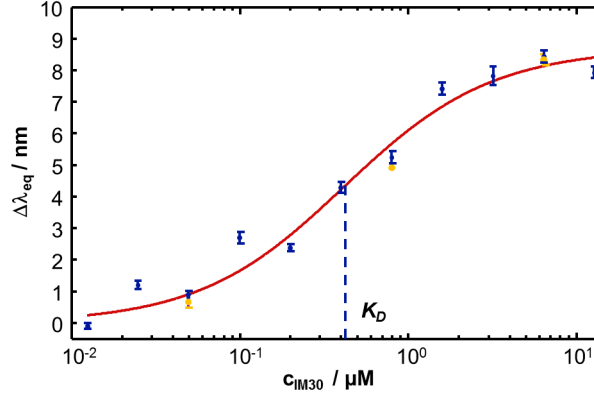


Figure 26: Thermodynamic dissociation constant determined via NanoSPR shows binding affinity for smaller ordered oligomers. Fitting $\Delta\lambda_{eq}$ measured for each concentration (blue: mean and standard error of 20-80 particles). With the Langmuir equation we obtain a dissociation constant for IM30 on Au@DOPG of $K_D = 0.42 \pm 0.02 \mu M$ with the calculations made above we claim, that this dissociation constant indicates the binding affinity of smaller ordered oligomers of IM30 or even protomers to PG-bilayers. Measurements of the equilibrium resonance wavelength shifts of a mutant that is not able to form ring structures (IM30_FERM, yellow), show the same binding affinity on our sensors and confirm this assumption.

To determine the dissociation constant K_D of IM30 and PG-bilayers the equilibrium resonance wavelength shift ($\Delta\lambda_{eq}$) of the adsorption of different IM30 concentrations on Au@DOPG was measured. The dissociation constant was obtained by fitting this data with the Langmuir equation (11) and gave a dissociation constant of $K_D = 0.42 \pm 0.02 \mu M$ (Fig. 26) in comparison to the dissociation constant of IM30 on liposomes, which have a much bigger surface area, of $K_D = 7.20 \pm 0.95 \mu M$. [51]

$$\Delta\lambda_{eq}(c_{IM30}) = \Delta\lambda_{max} \cdot \frac{c_{IM30}}{K_D + c_{IM30}} \quad (11)$$

In addition to the IM30 wild type, also the adsorption of IM30_FERM, a mutant that exhibits drastic destabilization of the ring structures and have a binding affinity of around $K_D = 1.4 \mu M$ on liposomes, was measured on Au@DOPG for several concentrations and shows the same binding affinity to this type of sensors as the wild type. This results support the assumption that the adsorbed species on our nanosensors is not the high molecular mass oligomeric ring structure, but the lower-ordered structures, the protein can form. In addition to that one can see that the lower-ordered structures even bind with higher affinity and ring formation counteracts membrane binding, a fact that is very important to understand the function of this protein.

NanoSPR can be used to determine the adsorbed species of a protein

In this chapter I showed that except of the determination of binding affinities NanoSPR can elucidate the function of proteins and be a helpful tool in their characterization. I showed how to determine size and binding affinity of an adsorbed species from the same experiment. In the case of IM30, a protein that forms oligomeric ring structures with high molecular weight, it was possible to identify the lower ordered oligomers or even protomers as adsorbing species on lipid bilayers with higher binding affinity. Even though the equilibrium for oligomerization lies nearly completely on the ring structure side, by calculating the plasmon shift that these rings would induce and comparing this to our adsorption curves, we can see that less than 25% of the shifts measured could be caused by ring binding, with complete disregard to concentration effects, which would even lower this percentage. The data was validated with a mutant that is not able to form complete ring structures showing the same binding affinity to our nanosensors as the wild type protein. This project was the first time, that NanoSPR found an application to clarify a biochemical question and manifests the advantages of using a small sensors, whose size is approaching the size of the analyte. Since our measurements are done in a label free way, we can additionally exclude that our results are influenced by, for example, dyes. To improve this method and make it more sensitive to the exact size of an adsorbed species, the measurements can be modified to detect single particle plasmon resonance wavelength time traces, where for sufficiently low analyte concentration the shift for a single analyte adsorption event can be measured. This can make it possible to determine whether the protein adsorbs as protomers or as lower ordered oligomers with a defined number of protomers.

Gold Nanorods as Plasmonic Sensors for Particle Diffusion and Surface Interactions

Abstract

Plasmonic gold nanoparticles are widely used as sensor to detect surface coverage changes. If the interactions between an analyte in solution and the nanosensor surface are negligible, the analyte diffuses through the sensors sensing volume without attaching. The diffusion of an analyte through the sensing volume results in a small fluctuation of the plasmon resonance wavelength. The sensing volume of a gold nanoparticle is in the order of its own volume, i.e. in the attoliter regime. The measurement of these fluctuations require a combination of high time resolution, spectral precision, and a high setup stability over the measurement time, which we achieve with a modified optical dark-field spectroscopy setup which allows a spectra read-out of 12,500 *fps*. We demonstrate successfully the feasibility of this technique on small gold and polystyrene nanoparticles as diffusors. We extract diffusion coefficients from our fluctuating plasmon resonance signal using a theoretical model that we developed and investigate the effects of diffusor-size, viscosity of the solution, and diffusor-concentration. I was able to show that the obtained diffusion coefficients follow the Stokes-Einstein equation, validating the applicability of the technique. Comparing the results from our technique with those obtained by dynamic light scattering (DLS), we get insights in the extend of the viscous drag the diffusors suffer from the flow-cell as well as from the nanosensor's surface. We are able to show that our measurements are independent on the chemical composition of the diffusors and the ionic strength of the medium. The work on this project included reestablishing, stabilization, and characterization of the setup, as described in a previous section. Theoretical modeling and the outcoming fitting function was contributed by Fabian Knoch from the group of Prof. Dr. Thomas Speck (Institute of Physics, Mainz).

A variety of techniques to detect diffusion of particles has a variety of potentials

Knowledge on diffusion behavior of particles or molecules is very important to get insights into reaction kinetics, inter-particle or particle-surface interactions or simply the size of the diffusors. A common and attractive approach to detect particle diffusion is to label the diffusors with fluorescent dyes, plasmonic metal nanoparticles or quantum dots and track their fluorescent or scattering intensities in a certain observation volume over time. The measurement principle to determine the diffusion time of an analyte is always the same: A fluctuating signal, for example from a fluorescent dye entering and leaving a defined volume is measured over time. Making sure that only a few analytes are in this sensing volume ensures resolving the density fluctuations of single analytes. By an autocorrelation of the signal, the mean lag time of a single analyte in the sensing volume can be extracted. At present, the most routine tool to investigate these dynamics is fluorescence correlation spectroscopy (FCS),^[61] but also its equivalent resonance light scattering correlation spectroscopy (RLSCS)^[62] or confocal correlation spectroscopy (CCS),^[63] where plasmonic particles or quantum dots are used as labels, have been proven to be suitable to study particle behavior. Apart from the variety of labeling-techniques there exist also different geometries of sample illumination, ranging from confocal laser beams over dark-field illumination to total internal reflexion (TIR) geometries, where the two latter ones permit spatially resolved measurements.^[64, 65] A TIR-illumination geometry is also suitable to not exclusively detect diffusion in solution, but to extract kinetic constants for an interaction between the analyte and the surface.^[66] All these techniques require labeling of the analyte, which has many disadvantages such as bleaching, blinking, blocking of binding sites or simply the increase in analyte size impairing the native diffusion behavior. An alternative label-free method is dynamic light scattering (DLS), where the scattering intensity of the analyte itself is measured, but at high concentration DLS gives the collective diffusion coefficient instead of self diffusion. Another approach is to introduce a small sensor, in whose environment the diffusion can be detected.

Diffusion sensing with nanorods: A first step to detect surface interactions

A possible sensor to detect label-free analyte diffusion in its environment are nanorods having a sensing volume in the attoliter range. If interactions between an analyte in solution and the nanosensor surface are negligible, the analyte diffuses through the sensing volume resulting in small fluctuations of the plasmon resonance wavelength, due to a change in the dielectric environment of the nanosensor. The time a diffusor remains in the sensing volume of a nanosensor is dependent on its diffusion coefficient and the size of the sensing volume, but for nanorods always in the sub-millisecond regime. Thus resolving these fluctuations demands a microscope setup, that allows for high time resolution and high measurement stability, as I showed in a former section it is the case for the TIR-setup. In this section I

prove the feasibility of these measurements using a model system of single immobilized gold nanorods as sensors and gold and polystyrene nanoparticles as diffusors to show that by measuring the plasmon resonance wavelength of a nanosensor with high time resolution, we can detect particle diffusion in its nearby surrounding as fluctuation in the signal. Using a theoretical model that we developed and investigating the effects of diffusor-size, viscosity of the solution and diffusor-concentration, it was possible to show that the obtained diffusion coefficients follow the Stokes-Einstein equation. With these results, we demonstrate that plasmonic sensors are suitable to give insights into the Brownian dynamics of unlabeled macromolecules.

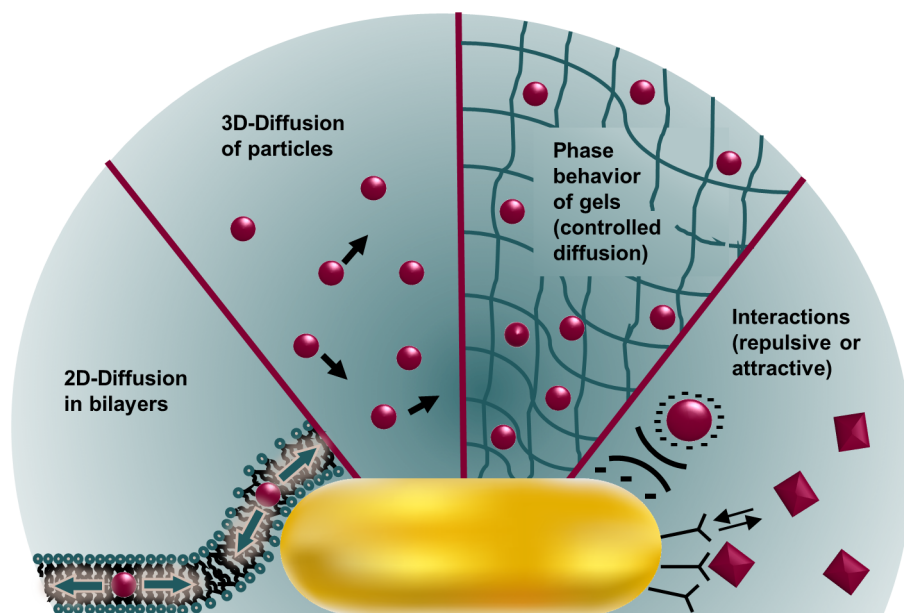


Figure 27: Scheme of possible applications of diffusion sensing by nanorods.

Possible fields for application are diverse (Fig. 27): It is possible to determine three dimensional self-diffusion of analytes and obtain their hydrodynamic radius. As we are able to cover our particles with lipid bilayers, also density fluctuations in their layer, e.g. caused by membrane proteins diffusing in two dimensions, and with this the phase behavior of the lipids can be investigated. Apart of lipid bilayers also phase transition measurements of polymeric gels are a possible application. Here the diffusors would work as a labels and should move faster above the phase transition temperature of the polymer. As we are using a sensor whose surface can be either charged and/or functionalized with a certain recognition element specific for an analyte, it is also possible to extent this method by taking surface interactions (repulsive or attractive) into account. Measuring in thermodynamic equilibrium the coverage of the surface fluctuates with a frequency dependent on the interactions between the

surface and the analytes, but much lower than it is the case for pure diffusion. Knowing the diffusion time of particles near the surface we can identify interactions as a kind of dwell time.

Setup time resolution is sufficient to measure diffusion of particles

Free diffusion of particles in solution is defined by a particle type specific diffusion coefficient D and follows the Stokes-Einstein equation (eq. 12). The diffusion coefficient is dependent on the system temperature T , the viscosity of the medium η and the hydrodynamic radius of the diffusers R_H , which is influenced by the nanoparticle coating and also solvent effects.

$$D = \frac{k_B T}{6 \pi \eta R_H} \quad (12)$$

The diffusion time τ_D is described in the Einstein-Smoluchowski equation for a random walk in one dimension with the mean square displacement $\langle x^2 \rangle$ of a particle in a certain time.

$$\langle x^2 \rangle = 2 D \tau_D \quad (13)$$

From these equations we can calculate the diffusion time particles with a certain size need to cross a volume with a dimension x and estimate if we measure fast enough to resolve the events of a particle entering and escaping this volume (Fig. 28a).

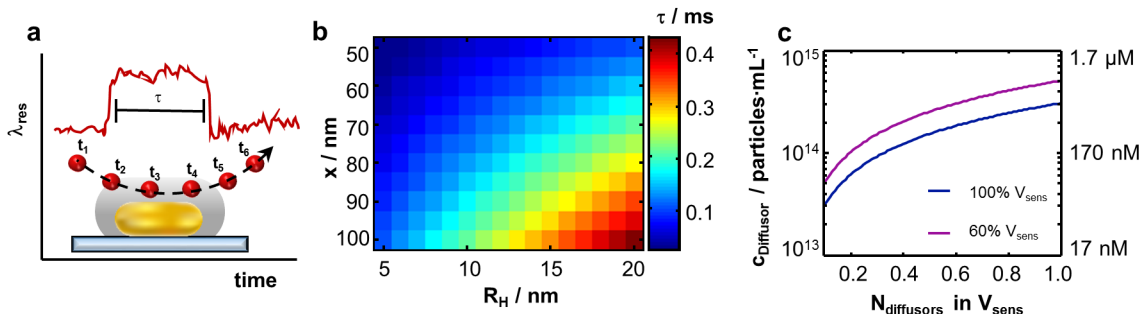


Figure 28: Theoretical considerations on possibility of diffusion measurements. a) The diffusion time is the time a particle needs to cover a certain distance, in our case the dimension of the sensing volume of a nanosensor. b) Diffusion time τ_D dependent on the length of a sensor x and the hydrodynamic radius R_H of a diffuser, calculated with the equations above. The diffusion time gets longer for bigger sensors and bigger diffusers. c) Calculated diffuser concentration for the number of particles in the whole sensing volume of a nanosensor with a diameter of 50 nm and a length of 100 nm (blue) and for 60% of the sensing volume (magenta), the part that is accessible when the sensor lies on the flow-cell surface. The optimal diffuser concentration is in the nM up to μM range.

For measurements of fast dynamics with the TIR-Setup we are limited to a minimum exposure time of $t_{ex} = 60 \mu s$, together with the time we need for spectral read out, we end up with a time resolution of $t_{measure} = 80 \mu s$. Our nanorod sizes are in the range of $15 - 50 nm$ in width and around $30 - 100 nm$ in length. If we relate the diffusion time to the dimension of the sensor (in this case only a mean dimension) and the hydrodynamic radius of the diffusers, we can get an idea on how we have to select a measurable model system by the sensor size and the diffuser size. In principle, the diffusion time is longer for bigger sensors and bigger, thereby slower, diffusing particles (Fig. 28b). Assuming that to resolve a certain diffusion time τ_D we need to measure with a time resolution of at least $t_{measure} = 1/2\tau_D$. To measure diffusers for example with a hydrodynamic radius of $10 nm$ we would need sensors with a mean dimension of $> 80 nm$. However, these rough estimations are done only for a simple one dimensional random walk and only serve to see if the timescale is sufficient.

To resolve diffusion of single particles, we need a certain amount of diffusers in the sensing volume. If the diffuser concentration is too high, we can not resolve single particle fluctuation, if it is too low the probability, that an event takes places gets rare. An average number of diffusers in the sensing volume of $N_{Particles} = 0.1 - 1000$ is stated for FCS measurements. In fluorescence correlation spectroscopy the sensing volume is about one femtoliter, which corresponds to concentrations between sub-nanomolar and micromolar.[67] The sensing volume of a nanorod is dependent on the particle dimensions, but generally in the attoliter range. To measure with an average number of particles between $N_{Particles} = 0.1 - 1$ in the sensing volume of a nanosensor with a width of $50 nm$ and a length of $100 nm$ having a sensing volume of $V_{sens} = 3.6 aL$ we need a diffuser concentration in the nM up to μM range (Fig. 28c).

Choosing sensor particles: The bigger the better

When characterizing the setup and its noise, we showed that particles with higher intensity have less noise. As the scattering intensity of nanoparticles is dependent on their volume $I_{sca} \propto V^2$ using big particles for our plasmon fluctuation measurements is favorable in terms of noise but also, as showed above, concerning our time resolution and the diffuser concentration. The diffusion time is dependent on the particle dimension, the bigger the volume they can diffuse through, the slower the diffusion time. To make sure that self diffusion of particles is not influenced by interparticle effects due to high concentrations, we should keep the particle concentration as low as possible, but still high enough to have an average of $0.1 - 1$ particles in our sensing volume. For my measurements I chose nanorods with a width of $w = (37.76 \pm 2.95) nm$ and a length of $l = (85.59 \pm 13.95) nm$ having a sensing volume of $V_{sens} = 1.8 aL$. The resonance wavelength of these particles is $\lambda_{res} = 644.8 nm$, which is in the range where the quantum efficiency of our camera is highest.

Fluctuation measurements and signal autocorrelation

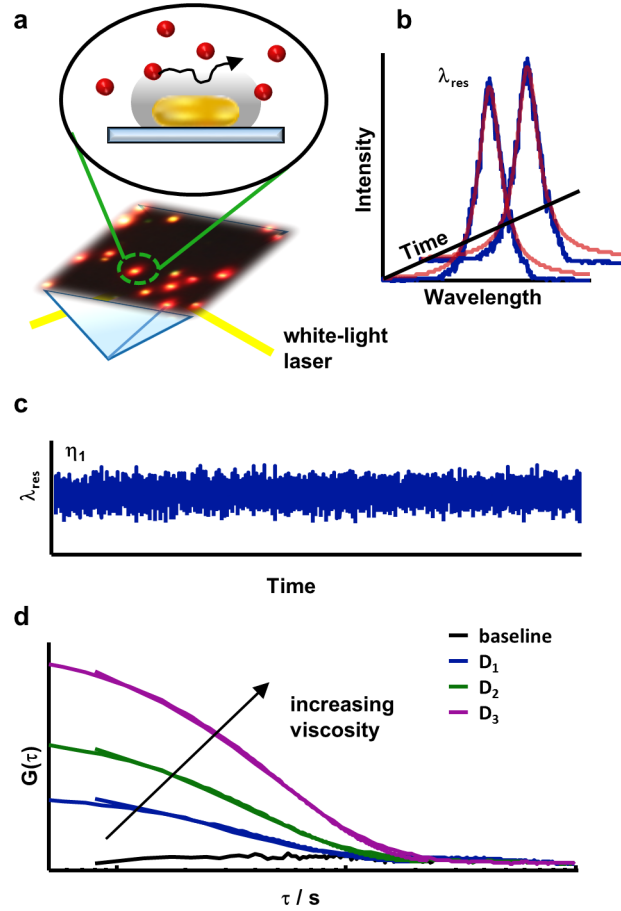


Figure 29: Measuring particle diffusion as plasmon resonance fluctuations. a) Nanosensors are deposited on a flow-cell surface and illuminated by the evanescent field created by a white-light laser coupled into a prism in total internal reflection geometry. Diffusors in the flow-cell medium pass the sensing volume of the nanorod without attaching. b) Single particle spectra are recorded with a frame rate of 12,500 *fps* and the plasmon resonance resonance wavelength λ_{res} for each frame is determined by a Lorentzian fit. c) From the time-trace of a fluctuating plasmon resonance wavelength we can not identify the presence of diffusor. d) The autocorrelations of λ_{res} measured with diffusors in medium with increasing viscosity shows a clear difference in diffusion behavior. The baseline is completely uncorrelated (black line).

The diffusors change the polarizability in the nearby environment of the plasmonic nanosensor, which results in fluctuations of its plasmon resonance wavelength ($\delta\lambda_{res}(t) = \lambda_{res}(t) - \langle\lambda_{res}(t)\rangle$). For our

measurements the sensors are deposited on a glass flow-cell surface and illuminated with a white-light laser in a total internal reflection (TIR) geometry (Fig. 29a). Because of the TIR-illumination geometry only the scattered light is collected by the objective of a microscope and detected by an electron multiplying charge-coupled device (EMCCD) coupled to a transmission spectrometer. This microscope setup allows us to measure the sensors with an exposure time of $60 \mu s$ and a total spectra read-out of $12,500 fps$. These high time resolutions are required to resolve the diffusion of particles in nanometer sized volumes. The spectra are fitted with a Lorentzian fit to obtain the plasmon resonance wavelength of the sensor for each frame (Fig. 29b). The normalized autocorrelation is calculated as

$$G(\tau) = \frac{\langle \delta\lambda(t + \tau)\delta\lambda(t) \rangle}{\langle (\delta\lambda)^2 \rangle} \quad (14)$$

Although our signal is overlaid by noise (Fig. 29c), we can see a difference of the diffusion behavior of particles in media with different viscosities in the calculated autocorrelations (Fig. 29d). The baseline without diffusors shows that our noise is completely uncorrelated. From analysis of these autocorrelations with a fitting function we can obtain the diffusion time of the particles in their medium, in this case glycerol in water in different ratios. To make sure that we do not measure any solvent effects, e.g. convection currents, we measured baselines of the nanosensors in absence of diffusors in water and in the glycerol/water mixtures used (see appendix). To verify that changes in scattering resonance wavelength are not caused by background scattering from the diffusing particles, the background signal was also investigated concerning its temporal correlation (see appendix).

Theoretical model enables sensor calibration

To extract information from the autocorrelation a mathematical model was applied, that is similar to the model applied to other correlation spectroscopy methods. The model includes the geometry and dimensions of the nanosensor and the resulting effective Volume V_{eff} , where the diffusors can diffuse through independently from each other. In principle a particle can diffuse in two different dimensions: Laterally in and out the sensing volume with an aspect ratio α , defined by the measurements of the sensor with a lateral length $r_0 = \sqrt{w \cdot l}$, with a diffusion time τ_{\parallel} and vertically, perpendicular to the sensor surface with a diffusion time τ_{\perp} that is dependent on the penetration depth of the electric field of the plasmon into the medium z_0 . The fitting function for the calculated autocorrelation reads

$$G(\tau) = A \cdot H(\tau/\tau_{\parallel}, \alpha)Z(\tau/\tau_{\perp}) \quad (15)$$

where H describes lateral and Z describes perpendicular diffusion (see appendix for explicit expressions). The prefactor A describing the amplitude of the autocorrelation includes the detector noise, whose temporal correlation is shorter than the resolution of the measurement and leads to an apparent

amplitude for our signal of $G(0) < 1$. This prefactor is not further interpreted. From the fitting function we obtain three parameter: A parameter included in the amplitude c_0 , the diffusion time τ_{\parallel} and the ratio (z_0/r_0) . From the latter two and the following relations we can obtain the diffusion coefficient D and τ_{\perp} if at least one dimension (z_0 or r_0) of the sensor is known.

$$\tau_{\parallel} = \frac{r_0^2}{4D}, \quad \tau_{\perp} = \left(\frac{z_0}{r_0}\right)^2 \tau_{\parallel} \quad (16)$$

The sensors can also be calibrated with an analyte, whose diffusion coefficient is known, a principle that is used to calibrate the lateral expansion of a laser beam in FCS. For our measurements we can use two different approaches: On the one hand we can calibrate the sensor with diffusion coefficients for the measured particles obtained from another method, like dynamic light scattering, and determine r_0 and z_0 that can now be taken as fixed parameters for other measurements with these sensors. On the other hand we can set r_0 and z_0 according to the measurements of the nanosensor (r_0) and their sensing distance (z_0) respectively obtained by evaluation of TEM-images and calculate the diffusion coefficients that way. With the first method we assume that the diffusion coefficients obtained by DLS and our method are the same. Independently on exact values for r_0 and z_0 we can validate our method by having a look on the fitting parameter, the diffusion time τ_{\parallel} .

Determined diffusion time τ_{\parallel} shows the expected dependency on viscosity η and independence on diffusor concentration c

To validate our system we investigated the influence of the viscosity of the solution and the diffusor concentration on the diffusion time τ_{\parallel} . We synthesized gold nanospheres with a mean particle diameter of 20 nm and coated them with methoxy polyethylene glycol (Au@mPEG) to make sure that these diffusors do not attach neither to the glass surface of the flow-cell nor to the sensors. In fact an absolute shift in the plasmon resonance wavelength of the sensors after flushing in the diffusors in the flow-cell was not observed indicating that attachment does not take place. The viscosity η of the solution was varied by an increasing glycerol/water ratio of the solution the diffusors are flown in. We measured the diffusors in 5%, 15%, and 25% glycerol in water, resulting in viscosities of $\eta_{5\%} = 1.075\text{ mPas}$, $\eta_{15\%} = 1.50\text{ mPas}$ and $\eta_{25\%} = 2.10\text{ mPas}$, respectively. For the diffusors in 15% glycerol ($\eta_{15\%} = 1.50\text{ mPas}$) we varied also the relative concentration c_{rel} of the particles from 1; 0.5; 0.25, all corresponding to particle concentrations in the nM range. For each sensor three trajectories over 20 s were recorded, and the fluctuating plasmon resonance wavelength was autocorrelated as described above and evaluated with equation (15) to obtain the diffusion time τ_{\parallel} as fitting parameter.

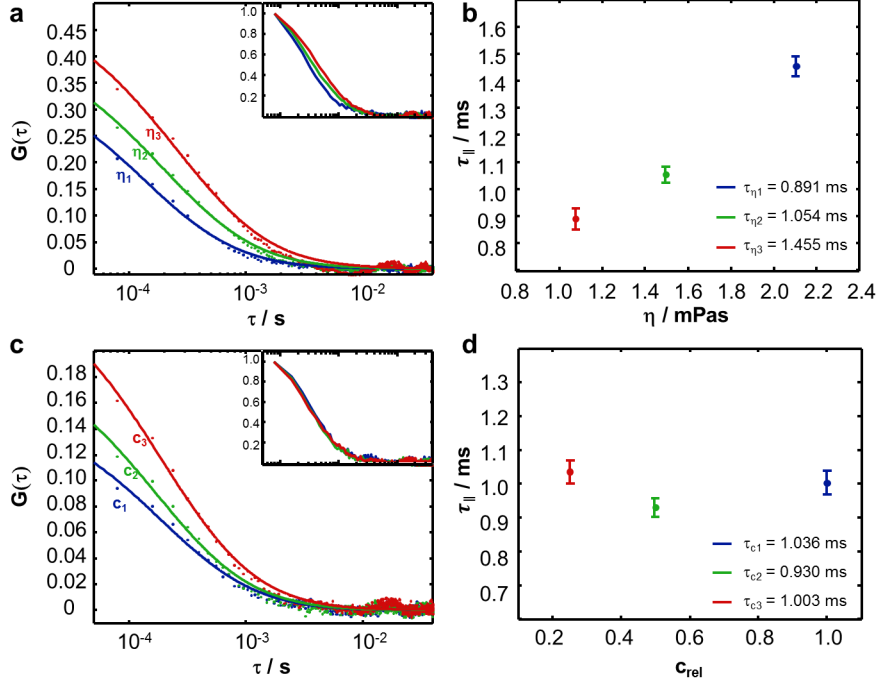


Figure 30: Diffusion times $\tau_{||}$ show the expected dependency on η . Measuring gold nanoparticles as diffusers in media with varying viscosity (a) and in different diffuser concentration (c) shows similar behavior. An increased viscosity η and an increase in concentration c show both an increase in the amplitude of the autocorrelation. A change in the diffusion time $\tau_{||}$ can be made obvious when normalizing the autocorrelation on $G(1)$ (insets in a and c). While at an increased viscosity the diffusion time increases as well, by changing the concentration it stays constant. The mean diffusion times and its standard deviation over all diffusers obtained from the fits are shown in (b and d).

In Figure 30 examples are shown for the autocorrelations and their corresponding fits from single nanosensors for the varying viscosities (Fig. 30a) and varying diffuser concentrations (Fig. 30c). For both figures we can observe the same trend, increasing viscosity and increasing concentration show both an increase in the amplitude of the autocorrelations, mainly induced by an increase in noise. However, normalization of the autocorrelation curves depicts that they differ in shape: An increase in viscosity is clearly shifting the diffusion time of the diffusers, an increase in diffuser concentration does not show any change (insets in Figure 30 a and c). To quantify these findings, the mean diffusion times from all measured time traces are shown (Fig. 30 b and d) and follow the expected trend: A medium with higher viscosity slows down the particles resulting in a higher diffusion time $\tau_{||}$, while a change in concentration has no influence on the diffusion time. For the ratio (z_0/r_0) , we consistently obtain $(z_0/r_0)^2 = 0.076 \pm 0.002$ for these measurements, which is independent from viscosity and

concentration, indicating that this ratio is a property of the nanosensor. As we measure diffusion close to a wall (the flow-cell surface as well as the sensor surface), we can not assume our diffusion coefficient being comparable to the one obtained by DLS. In fact the diffusion coefficient starts to drop tremendously when measured closer than $10 \mu m$ to a surface.[68][69] Therefore we do not calibrate our sensor dimensions with the help of diffusion coefficients measured via DLS, but calculate the diffusion coefficients with the help of the measurements of the sensor. The decay length of the electric field z_0 should reflect the decay of the sensitivity d_s , the calculated sensing distance of a plasmonic nanosensor with this size is $d_s = 16.1 nm$. With the fitting parameter $(z_0/r_0)^2$ we result in a value for $r_0 = 58.4 nm$, the same value calculated from the measurements of the sensors given above $r_0 = \sqrt{w \cdot l} = 56.8 nm$. The values z_0 and r_0 obtained by the theoretical model are the same calculated for the sensing distance and the dimensions measured for the particles.

Diffusion close to a wall is slowed down due to an increased viscous drag

When moving close to a wall of a container equation (12) has to be corrected because of the increased viscous drag caused by sheer stress. The parallel diffusion coefficient decreases and is reduced by[68]

$$D_{\parallel}(h) = D_{\parallel 0} \left(1 - \frac{9}{16} \left(\frac{a}{h} \right) + \frac{1}{8} \left(\frac{a}{h} \right)^3 - \frac{45}{256} \left(\frac{a}{h} \right)^4 - \dots \right) \quad (17)$$

where a is the particle radius, h is the sphere center height of a diffuser compared to the flow-cell surface and $D_{\parallel 0}$ is the parallel diffusion coefficient in bulk. For a particle directly diffusing over the surface $a = h$ the parallel diffusion coefficient can be reduced by $D_{\parallel}(h) = 0.387 \cdot D_{\parallel 0}$ when considering the expansion until the fourth term. From experimental data a decrease of a factor of 10 was reported for measurements of diffusion coefficients close to a surface compared to diffusion in bulk.[64] Calculating the diffusion coefficient with $d_s = z_0 = 16.1 nm$ as decay length for the electric field and the ratio $(z_0/r_0)^2$ and τ_{\parallel} obtained as fitting parameters inserted in equation (16) we get diffusion coefficients that are reduced by a factor $D_{DLS}/D_{NanoPCS} = 10.85 \pm 1.01$ compared to the ones measured via DLS and are listed in table 1.

Table 1: Diffusion coefficients from DLS and NanoPCS.

% glycerol in water	$D_{DLS}/\mu m^2 s^{-1}$	$D_{NanoPCS}/\mu m^2 s^{-1}$	$D_{DLS}/D_{NanoPCS}$
5	10.65 ± 0.50	0.98 ± 0.04	10.86
15	7.97 ± 0.47	0.81 ± 0.02	9.83
25	6.61 ± 0.55	0.56 ± 0.01	11.80

Diffusion coefficients of different types of diffusors show consistency of the method

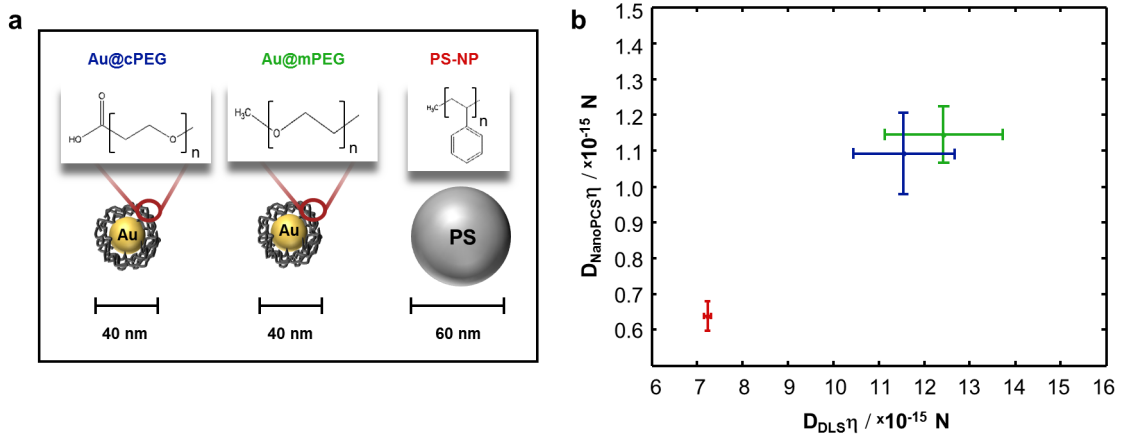


Figure 31: Diffusion coefficients of different particle types measured via NanoPCS are constantly smaller than in DLS. a) Diffusers measured on our sensors: Au@cPEG with a hydrodynamic radius of $R_H = (18.47 \pm 1.16) nm$, Au@mPEG with $R_H = (17.33 \pm 1.11) nm$ and polystyrene nanoparticles (PS-NP) with $R_H = (29.61 \pm 0.52) nm$. b) Diffusion coefficients normalized to the viscosity of the medium differ in a constant factor of $D_{DLS}/D_{NanoPCS} = 10.94 \pm 0.86$ due to the increased viscous drag of the flow-cell surface.

To verify that the variation in diffusion coefficients is not caused by specific diffuser properties like surface interactions between the mPEG functionalized diffuser surface and the nanorod we measured a variety of diffusers differing in surface coatings, size, and core material. We used methoxy-polyethylene glycol coated gold nanospheres (Au@mPEG) and carboxy-polyethylene glycol coated gold nanospheres (Au@cPEG) to test particles with different surface chemistry but comparable hydrodynamic radii $R_{H,Au@mPEG5kD} = 17.33 \pm 1.11 nm$ and $R_{H,Au@cPEG5kD} = 18.47 \pm 1.16 nm$ (size difference is only due to a slightly longer PEG-chain in the case of cPEG). Additionally we measured polystyrene nanospheres (PS-NP) with $R_{H,PS-NP} = 29.61 \pm 0.52 nm$ to investigate the size dependency and vary the core material of the particles (Fig. 31a). The hydrodynamic radii given above were obtained by DLS measurements. The different diffusers were also measured in medium with increased viscosities and the diffusion coefficients were calculated from the fitting parameter as described above using the same decay length of $z_0 = 16.1 nm$. All measurements were done at the same sensor surface at exactly the same sensor particles to ensure comparability of the results. All results from these calculations are summed up in the appendix (table 5-7). Normalizing the obtained diffusion coefficient to the viscosity of the medium gives a constant for each particle type, mainly dependent on the hydrodynamic radius $D\eta = \frac{k_B T}{6\pi R_H}$ (Fig. 31b). Correlating $D_{NanoPCS}\eta$ to $D_{DLS}\eta$ shows a linear dependency. Considering

the hydrodynamic radius of the diffusors as constant for both measurements, the viscous drag the diffusors suffer at the surface decreases the diffusion coefficient of a constant factor of about 10 (see table 5-7). The temperature for both systems was set to $T = 293\text{ K}$, which is the temperature at which DLS measurements were done. The exact temperature in the flow-cell is not known, but a change in temperature of $\Delta T = 100\text{ }^\circ\text{C}$ would change the diffusion coefficient by a factor of 0.03, which is in the range of the error of the measurement.

Increasing the ionic strength of the medium, does not influence measurements

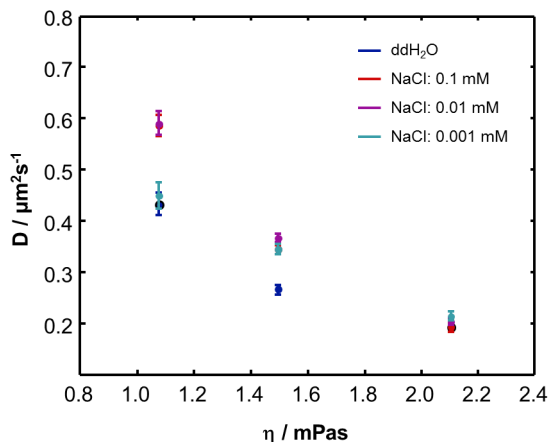


Figure 32: Diffusion coefficients of polystyrene nanoparticles measured in media with different ionic strength. PS-NP as diffusors were measured with increasing salt concentration. In ultra-pure water (blue), in 0.01 mM NaCl (turquoise), 0.1 mM NaCl (magenta), and 1 mM NaCl (red). Deviation in D does not follow any trend.

The ionic strength of a medium can have a high influence on particle surface interactions. Aggregation of the particles on the surface or between each other can take place when short range van der Waals interactions counteract the stabilization by electrostatic repulsion. Adding salt to a colloidal suspension decreases the electrostatic repulsion in a range dependent on the surface potential of the colloid and the number of ions in solution, an effect that is described by the DLVO-theory. If these interactions played a role in our measurements surface interactions between diffusor and sensor would change the diffusion behavior close to our sensors. An increase in ionic strength means a decrease in electrostatic repulsion and a diffusor could come closer to the sensor surface and even attach. However, increasing the ionic strength in a suspension of polystyrene nanoparticles from ultra pure water to 1 mM NaCl, a concentration where still no particle attachment on the flow-cell surface was observed, does not show

any systematic change in the diffusion coefficient. All particle types measured here have a negative zeta-potential (Au@mPEG and Au@cPEG: $\zeta \sim -35\text{ mV}$; PS-NP: $\zeta \sim -60\text{ mV}$), ensuring that no attachment on the negatively charged flow-cell and on the nanorod takes place. Particles with ζ -potential $> -20\text{ mV}$ tend to attach to the flow-cell surface, as observed for Au@mPEG particles in presence of sodium chloride. If interactions between diffusor and sensor are not negligible anymore but the system is in thermodynamic equilibrium one can determine the rate constants for adsorption and desorption from the fluctuating resonance wavelength, which is reflecting the coverage fluctuations of the nanosensor.[35]

Diffusion sensing can be expanded to investigate surface interactions

Gold nanoparticles already find their application in many fields, especially in biomedical applications. Inserting them in biological environments for example for drug delivery their interaction with all kinds of biological media is a crucial point. This interaction can be simple adsorption, but also fast/weak interactions contributing to the fate of the particle, where especially its point of destination and acting is something that wants to be controlled. Here I showed that we have the possibility to measure diffusion of an analyte close to the gold nanorod surface, that happen on short time scales. For our model system, we can see that interactions are negligible, as ionic strength as well as the chemical composition of our diffusors do not influence the diffusion coefficient. Differences in diffusion behavior close to our nanosensor and the flow-cell surface compared to diffusion in bulk can therefore be ascribed to the viscous drag of the wall. Knowing the contribution of this effect, we can now assign differences towards our 'free' diffusion to diffusion influenced by attaching and desorption on the nanosensor. The frequency of these interactions is dependent on the binding affinity k_{on}/k_{off} of a certain system. The weaker the binding the faster the interactions. As we showed that we are able to measure fast dynamics, we would be able to identify even weak surface-particle interactions, something that is interesting for example in material science to determine the quality of anti-biofouling surfaces.

Part III

Summary

In the last years single nanoparticles, in particular gold nanorods, as sensors in dark-field microscopy and micro-spectroscopy legitimate their use to tackle biophysical and biochemical questions. Because of their small size, one can create a sensor platform containing thousands of single sensors, in principle each with a specific surface coating responsive to a special analyte, as shown already for four single analytes. Going beyond simple detection we can characterize binding affinities of analytes and as shown in this thesis even fast dynamics, e. g. particle diffusion, are not longer impossible to detect and to characterize.

Being 'in business' such a long time single nanoparticles are still not characterized experimentally concerning the distance dependency of their sensitivity. Especially the most relevant question in adsorption experiments, how a layer of recognition elements influence the plasmon resonance wavelength shift upon adsorption of an analyte, lacks of systematic studies. Answering this question can help to find an optimal sensor and to determine a molecular detection limit for a certain system. As an approach to solve this question I offered silica coated gold nanorods as sensors, whose sensing distance can be blocked with a shell having a defined thickness. I showed that these shells are sufficiently homogeneous to be suitable tools to model adsorption upon a layer around the particle. Disadvantageous for sensitivity measurements, but useful for sensing of analytes in crowded and multi-component solutions, is their porosity. A porous sensor is able to exclude analytes exceeding a certain molecular weight cut-off (MWCO), i.e. a certain size, from coming close to the sensor and being detected. A principle that can be used in multiplexed sensing as preselection step and that can reduce cross-talk between analytes and receptors not meant to be specific for each other. A successful test was done with BSA, which escaped sensing being too big to enter the pores of the silica shell, while bare particles in the same flow-cell detected its presence. A useful side-effect from this MWCO is that silica coated nanorods can be used as plasmonic reference particles in single-wavelength measurements. I showed that a silica shell thickness exceeding the sensing distance of the particles, makes them inert against changes in their dielectric environment. Thus, changes in their scattering cross sections are not due to changes in their plasmon, but artifacts from the measurements. The measurements done here do not exceed the level of proof-of-principle, but open the door to further experiments and studies. Besides we can see that a sensor whose properties seem to be completely disadvantageous for sensing (blocking of the sensing volume by a shell) can still find versatile applications.

Using theoretically calculated values for the sensing distance, I was able to extend NanoSPR, a method to characterize binding affinities of protein-protein interactions similar to surface plasmon resonance spectroscopy, to biosystems that coexist in various sizes. Nature provides proteins that are able to

oligomerize amongst each other or with other proteins, either as a storage form or to build up a reactive species. One of these proteins is IM30, a protein abundant in plants and cyanobacteria and was used for this project. As IM30 does not react with a receptor, but with a negatively charged lipid bilayer, I successfully coated the particles with these agents resulting in stable particles even in buffer. Enduing a nanoparticle with lipids and performing adsorption experiments, I identified from the magnitude of the plasmon resonance wavelength, which correlates to the size of the adsorbed analyte, the reactive species of an oligomer forming protein, elucidating the function of this protein. Characterization of the reactive species of a biological system is very often a problem, because of the small size of most of the proteins, which enables them to escape analysis, especially in imaging techniques. Having a sensor that is adaptable to measure the size of an analyte is a helpful tool in the investigation of protein function. Assuming a protein dimer to have double the size of a protomer, a small sensor can differentiate between those two upon single analyte adsorption.

Delivery of analytes towards the sensor is diffusion driven. Measuring in thermodynamic equilibrium and with a sensor-analyte system whose interactions are negligible, we can detect pure particle diffusion close to the nanosensor surface of analytes crossing the sensing volume of a nanosensor with the precondition that we measure fast enough. Having a sensing volume in the attoliter range the diffusion time of a particle is in the micro- to millisecond regime. To measure this diffusion, I improved and characterized a yet existing setup and tuned it to high time resolution measurements. The feasibility of the method was successfully shown on a model system of gold and polystyrene nanoparticles as diffusors and influences like solution viscosity, salt concentrations and diffusor concentrations were investigated. The results showed that we can determine the increased viscous drag the particles suffer close to a surface. These diffusion measurements and their characterization are the first step to determine surface interactions. As soon as surface interaction start to play a role, the diffusion time differs strongly, i. e. slows down compared to pure diffusion. Yet suffering from a technically limited time resolution, our setup is still able to measure the surface coverage fluctuations of an analyte adsorbing and desorbing at the sensor surface in thermodynamic equilibrium of the system. Measuring these fluctuations delivers the kinetic constants and thus the binding affinity between an analyte and the surface from one single experiment and without the unintended effect of mass transfer.

Part IV

Appendix

Silica-coated gold nanorods as sensors

Materials

Deionized water from a Millipore system ($>18\text{ M}\Omega$, MilliQ) was used in all experiments. Cetyltrimethylammonium bromide (CTAB) was purchased from Fluka, tetraethyl orthosilicate (TEOS) and *bovine serum albumin* (BSA) were purchased from Sigma, sodium hydroxide was purchased from Merck. Methanol and glycerol were purchased from Carl Roth.

Silica coating of gold nanorods

The thickness of the silica shell was modified via the CTAB concentration in the reaction tube.[47] To control the CTAB concentration in solution gold nanorods were washed once with water, centrifuged again and resuspended in 1.5 mL of a certain CTAB solution ($0.3 - 1.2\text{ mM}$ in water) to a final particle concentration of 2 nM . The suspension was left stirring over night to equilibrate. Then $6\text{ }\mu\text{L}$ of NaOH (0.1 M) were added to set a pH between 10 to 11. After a further 30 min of stirring, $13.5\text{ }\mu\text{L}$ of TEOS (20% v/v in methanol) were added and the solution was left stirring for about 20 h at room temperature. The particles were centrifuged and resuspended in ethanol.

Calcination of the silica shell

Silica coated particles are highly stable in ethanol but a few nanometer of the silica shell can be washed away in water.[32] The stability in water can be improved by a high-temperature treatment. We calcinated the dried particles at $100\text{ }^\circ\text{C}$ for 1 h , which is a temperature where no reshaping of the particles is observed but the particles become stable in water up to a few days.[50] The dried powder of the silica coated particles can be stored and the particles can be easily resuspended in water or ethanol.

NanoSPR for Oligomer-forming Proteins

Materials

Deionized water from a Millipore system ($> 18 M\Omega$, MilliQ) was used in all experiments. IM30 and IM30_FERM, as well as the Hepes-buffer and DOPG-lipids were obtained by the group of Prof. Dr. Schneider. CTAB gold nanorods were not synthesized, but taken from the batch used in [30]. 7K zeba spin columns were purchased from Thermo Scientific, poly-L-lysine hydrobromide and agarose for gel-electrophoresis were purchased from Sigma.

Preparation of DOPG-lipids

Lipid films of DOPG are prepared in chloroform, dried under nitrogen stream in a $38^\circ C$ water bath followed by 4 h under vacuum at $40^\circ C$. Vesicles were obtained by swelling the lipid film in water or buffer solution (Hepes $20 mM$) and 3 times alternating vortexing and sonication, each step for 3–5 min. The suspension was diluted to a concentration of $6 mM$ and vesicles were obtained by three cycles of freeze-thawing.

Preparation of DOPG functionalized particles

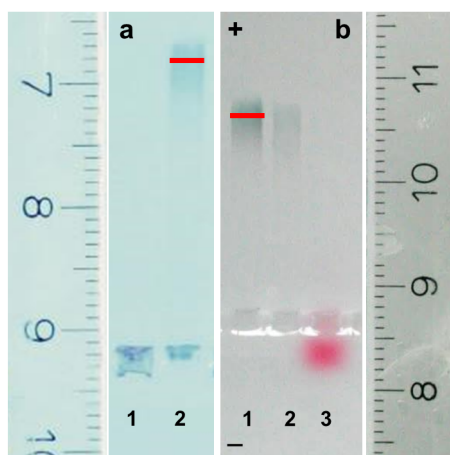


Figure 33: Gel mobility of DOPG-AuNRs shows successful functionalization and high stability. a) Au@CTAB aggregate in the well of the gel (1), while Au@DOPG show a high gel mobility because of their negative charge but some unfonctionalized particles are left (2). b) After filtration in a spin column less unfonctionalized particles are left (1) and the Au@DOPG particles incubated three days in working buffer (Hepes $20 mM$) keep their colloidal stability (2). Vitamin B was run as a control (3).

To replace the CTAB layer around the particles by a lipid bilayer, the Au@CTAB were centrifuged at 4020 *g*, and the pellet containing the Au@CTAB was resuspended in ultrapure water. The particle suspension was then mixed with liposomes with a high excess of lipids compared to the estimated surface CTAB concentration on the nanorods ($\sim 1 : 2,000$). Subsequently, Au@CTAB and the liposomes were incubated for 18 *h* at room temperature. To remove unfunctionalized particles and remaining lipids from the solution, Au@DOPG were separated on a 7K zeba spin desalting column (Thermo Scientific). UV/Vis spectroscopy and agarose gel electrophoresis showed that the resulting particles had a slightly different plasmon resonance position and a higher gel mobility compared to Au@CTAB, as expected when particles are coated with a lipid layer. The stability of the particles in working buffer was proven by incubating them during three days in Hepes 20 *mM*.

NanoSPR experiments

To attach the lipid-coated particles on the negatively charged glass surface of the microscope flow-cell, the flow-cell was incubated first with 0.1 *mg/mL* poly-L-lysine hydrobromide for 5 *min* and then thoroughly washed with 2 *mL* ultrapure water. Then, Au@DOPG were injected and incubated with the glass surface until an adequate surface density of attached particles was reached. Unbound particles were washed out. After rinsing with working buffer (20 *mM* Hepes, pH 7.6), the position of each deposited nanoparticle within the field of view was recorded. The particles left for about 30 *min* in buffer to stabilize. About 20 particles were randomly selected to be measured over 1 *h* while the protein was flushed in with a flow-rate of 75 $\mu\text{L}/\text{min}$. The plasmon resonance wavelength shift of every single particle was measured about every minute. At the lowest concentrations, the experiments were done 3-4 times for every IM30 concentration

Gold Nanorods as Plasmonic Sensors for Particle Diffusion

Materials

Deionized water from a Millipore system ($> 18 M\Omega$, MilliQ) was used in all experiments. Hydrogen tetrachloroaurate trihydrate (HAuCl_4) and sodium borohydride (NaBH_4) were purchased from Sigma. Cetyltrimethylammonium bromide (CTAB), and sodium citrate were purchased from Fluka. Glycerol, silver nitrate (AgNO_3) and hydrochloric acid HCl (37 wt. %) were purchased from Carl Roth. Ascorbic acid was purchased from AppliChem and sodium oleate (NaOL) was purchased from TCI. Polystyrene nanoparticles (PSNP) were purchased from micromod Partikeltechnologie GmbH.

Nanosensor synthesis and characterization

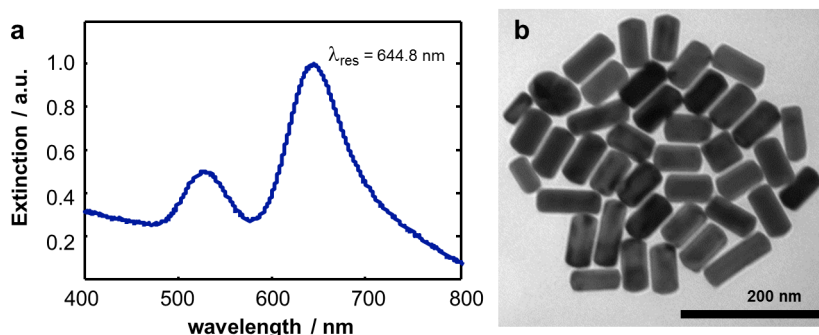


Figure 34: Characterization of the nanosensors. a) UV-vis spectroscopy displays a mean plasmon resonance of the nanosensors of $\lambda_{res} = 644.8 \text{ nm}$. b) The size of the nanorods extracted from TEM-images, shows a mean and a standard deviation for length of $l = (85.59 \pm 13.95) \text{ nm}$ and width of $w = (37.76 \pm 2.95) \text{ nm}$.

Gold nanorods were synthesized with a seeded-growth method using sodium oleate (NaOL) and CTAB as surfactants.[70] For the seeds 1 mL of a fresh 5 mM NaBH_4 was added under vigorous stirring to a solution containing 5 mL of 5 mM HAuCl_4 and 5 mL of a 0.2 M CTAB. When the solution color changed from yellow to brown, stirring was stopped and the seed solution was aged for 30 min .

To prepare the growth solution $360 \mu\text{L}$ of 4 mM AgNO_3 was added to 5 mL solution containing 0.077 M CTAB and 0.016 M NaOL and kept for 15 min at 36°C . Then 5 mL of 1 mM HAuCl_4 was added and stirred until the solution became colorless. $20 \mu\text{L}$ of HCl (37 wt. %) were added and after another 15 min , $25 \mu\text{L}$ of 64 mM ascorbic acid were added. In a final step $40 \mu\text{L}$ of the seed solution was added and the mixture was kept undisturbed at 36°C for 12 h . The gold nanorods were cleaned by centrifugation ($6,600 g$ for 10 min) and resuspended and stored in a 0.1 M CTAB solution. UV/vis

spectroscopy showed a plasmon resonance wavelength of $\lambda_{res} = 644.8 \text{ nm}$ (Fig. 34a) and from TEM-images we could extract their mean size and standard deviation of length $l = (85.59 \pm 13.95) \text{ nm}$ and width $w = (37.76 \pm 2.95) \text{ nm}$ (Fig. 34b).

Diffusor synthesis and functionalization

Polystyrene nanoparticles (PS-NP) with a diameter of around 50 nm were purchased from micromod Partikeltechnologie. Gold nanoparticles (AuNP) were synthesized following the Turkevich method:[71] 400 mL of 0.01% (w/v) HAuCl_4 were heated to boiling. Then 8 mL of 1% (w/v) sodium citrate was added under vigorous stirring. The solution was kept at boiling point until no further color change was observed and left stirred overnight at room temperature. For the functionalization of the diffusors with methoxy-polyethylene glycol (mPEG, 5kDa) and carboxy-polyethylene glycol (cPEG, 5kDa), respectively, the particle solution was centrifuged at $5,050 \text{ g}$ for 30 min in 50 mL centrifuge tubes to concentrate the particle suspension to a total volume of 4 mL . The respective PEG was added to the particles to obtain a final concentration of 1.5 mM and the solution was stirred overnight. The particles were then centrifuged at $10,300 \text{ g}$ and washed with water three times.

Refractive index measurements of glycerol/water mixtures

The refractive indices of the glycerol/water mixtures used for these experiments and all sensitivity measurements were measured in a refractometer at a temperature of $23.3 \text{ }^\circ\text{C}$ and are listed in table 2. For water the refractive index of $n = 1.33$ was used.

Table 2: refractive indices for the glycerol/water ratios.

% glycerol in water	n
5	1.3413
10	1.3491
15	1.3559
20	1.3640
25	1.3713
35	1.3967

Viscosimetric measurements

Viscosities of the glycerol/water mixtures were measured with a Couette-viscosimeter. I measured 5%, 10%, 15%, 20% and 25% (v/v) glycerol in water at a temperature of $21 \text{ }^\circ\text{C}$ and a velocity of 120 rpm

and 140 rpm for a measurement time of 40 s. The measurement was repeated three times for each glycerol/water ratio. Mean and standard deviation is summed up in table 3 for pure water a viscosity of $\eta = 1.005 \text{ mPas}$ was taken.

Table 3: Measured viscosities for the glycerol/water ratios.

% glycerol in water	η/mPas
5	1.075 ± 0.025
10	1.290 ± 0.000
15	1.495 ± 0.005
20	1.747 ± 0.005
25	2.103 ± 0.004

Determination of the hydrodynamic radius via dynamic light scattering

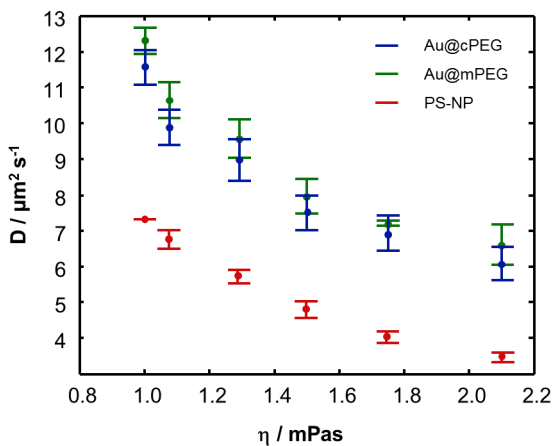


Figure 35: Mean diffusion coefficient and their standard deviation of the diffusers measured in dynamic light scattering. The diffusion coefficients were measured for different viscosities for the three types of diffusers: Au@cPEG-4.8kDa (blue), Au@mPEG-5.1kDa (green) and PS-NP (red). The gold particles were taken from the same batch, the difference in diffusion coefficient is only due to the different length of the PEG-chains.

Dynamic light scattering measurements were done with an illumination laser wavelength of 532 nm at three different angles simultaneously (110°, 90°, 70°). The particles were measured in different glycerol/water ratios (0%-25% glycerol) resulting in viscosities between 1.0 – 2.1 mPas (see table 3). As the measurements did not exhibit any significant angular dependency, diffusion coefficients are

denoted as mean and standard deviation over all angles (Fig 35). The mean hydrodynamic radii R_H of the particles in solution were obtained by solving the Stokes-Einstein equation (eq. 12) at every measured viscosity and taking the mean over the obtained values. All results are listed in table 4.

Table 4: Diffusion coefficients for Au@mPEG, Au@cPEG and PS-NP determined via DLS.

$\eta/mPas$	$D_{Au@mPEG}/\mu m^2 \cdot s^{-1}$	$D_{Au@cPEG}/\mu m^2 \cdot s^{-1}$	$D_{PS-NP}/\mu m^2 \cdot s^{-1}$
1.005	12.30 ± 0.35	11.57 ± 0.48	7.30 ± 0.00
1.075	10.65 ± 0.50	9.89 ± 0.49	6.75 ± 0.27
1.290	9.58 ± 0.53	8.98 ± 0.59	5.72 ± 0.18
1.495	7.97 ± 0.47	7.51 ± 0.48	4.79 ± 0.23
1.747	7.21 ± 0.08	6.95 ± 0.50	4.02 ± 0.17
2.103	6.61 ± 0.55	6.08 ± 0.47	3.47 ± 0.13
R_H/nm	17.33 ± 1.11	18.47 ± 1.16	29.61 ± 0.52

Explicit expression of Z and H

Diffusion perpendicular to the surface $Z(\tau/\tau_{\perp})$ is described by

$$Z(x) = e^{x/4} \operatorname{erfc}(\sqrt{x/4})(1 - x/2) + \sqrt{x/\pi}$$

and the lateral diffusion $H(\tau/\tau_{\parallel}, \alpha)$ with α being the aspect ratio of the particles is described by

$$H(\zeta, \alpha) = h_1(\zeta/\alpha)h_1(\zeta\alpha) + h_2(\zeta/\alpha)h_1(\zeta\alpha) + h_1(\zeta/\alpha)h_2(\zeta\alpha) + h_2(\zeta/\alpha)h_2(\zeta\alpha)$$

with

$$h_1(x) = \operatorname{erf}\left(\frac{1}{\sqrt{x}}\right); \quad h_2(x) = \sqrt{x/\pi} \left(e^{-\frac{1}{x}} - 1\right)$$

Background signal is uncorrelated and no medium effects are observable

The plasmon resonance wavelength fluctuation of the nanosensors in water and the glycerol/water ratios used to change the viscosity of the medium (5%; 15%; 25%) in the absence of diffusors were measured as baselines. The autocorrelations from these fluctuation indicate a totally uncorrelated background (Fig. 36).

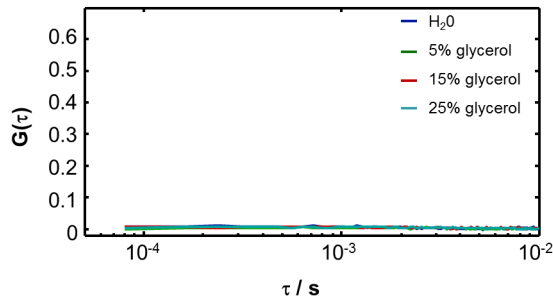


Figure 36: Baseline autocorrelations without diffusors. The autocorrelated plasmon resonance wavelength of the nanosensors without diffusors in different media are uncorrelated and do not exhibit any solvent effects.

The scattering intensity of the diffusors themselves does not influence measurements

To prove that the diffusors themselves are not illuminated in our setup and thus do not contribute with their scattering light to the signal from the plasmonic sensors, we selected areas on the flow-cell surface where no sensor particle was present as background (Fig. 37a). The scattered background light from these areas was detected over time. The mean intensity of the background over time is in four orders of magnitude lower than the intensity of a particle spectrum, which shows that the background signal can be neglected and that we can simply correct our spectrum by the offset of the camera (Fig. 37 b and c). Autocorrelating the intensities $I(t)$ of the background signal at two different wavelength ($\lambda_1 = 500 \text{ nm}$ and $\lambda_2 = 650 \text{ nm}$) we can clearly see that the scattered background light is uncorrelated and does not contribute to our signal (Fig. 37d).

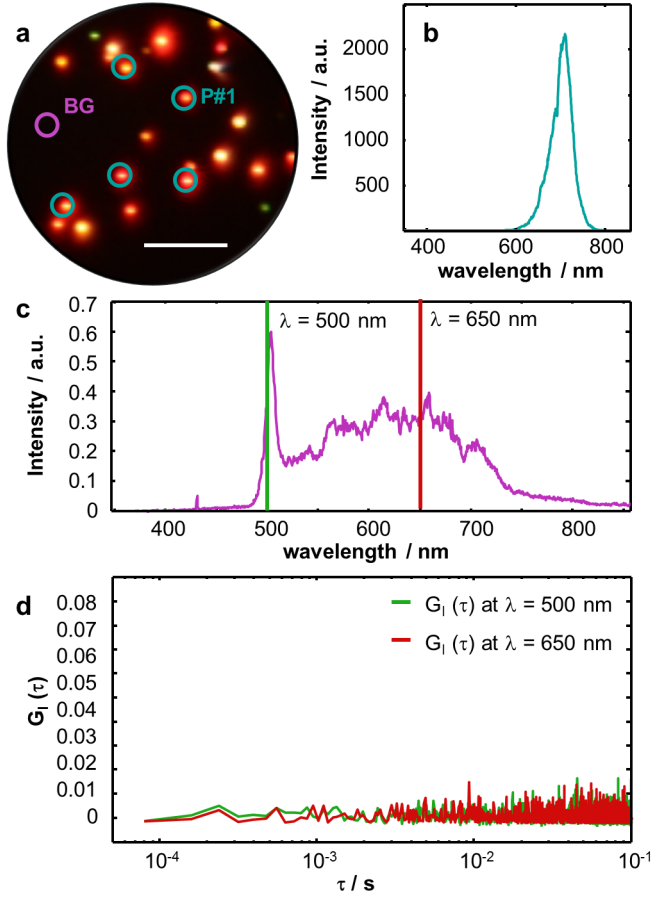


Figure 37: Control measurements for background scattering. a) The background scattering was measured at a place of the flow-cell surface free from particles (turquoise circle, scale bar is $50 \mu m$). b) The intensity of the background scattering is in the order of three magnitudes lower than the scattering intensity of the particle spectrum. c) Background intensity has the form of a white-light spectrum and the intensity over time autocorrelated at two different wavelength ($\lambda_1 = 500 nm$ and $\lambda_2 = 650 nm$). d) The autocorrelations of the two intensities over time show a completely uncorrelated scattering intensity and thus do not contribute to our signal.

Calculation of diffusion coefficients from fitting parameters:

Diffusion time $\tau_{||}$ and the ratios $f = (z_0/r_0)^2$ were obtained as fitting parameters. Diffusion coefficients were calculated with $r_0^2 = z_0^2 \cdot f^{-1}$ from equation (16) and are listed in table 5-7.

Table 5: Fitting parameters and calculated diffusion coefficients: Au@mPEG

$\eta/mPas$	$\tau_{ }/ms$	$(z_0/r_0)^2$	r_0/nm	$D_{NanoPCGS}/\mu m^2 s^{-1}$	$D_{DLS}/\mu m^2 s^{-1}$	$D_{DLS}/D_{NanoPCGS}$
1.075	0.891 ± 0.039	0.074 ± 0.001	59.18	0.983 ± 0.045	10.65 ± 0.05	10.84
1.495	1.054 ± 0.030	0.076 ± 0.001	58.40	0.809 ± 0.025	7.97 ± 0.47	9.85
2.103	1.455 ± 0.037	0.080 ± 0.001	56.92	0.557 ± 0.016	6.61 ± 0.55	11.87

Table 6: Fitting parameters and calculated diffusion coefficients: Au@cPEG

$\eta/mPas$	$\tau_{ }/ms$	$(z_0/r_0)^2$	r_0/nm	$D_{NanoPCGS}/\mu m^2 s^{-1}$	$D_{DLS}/\mu m^2 s^{-1}$	$D_{DLS}/D_{NanoPCGS}$
1.075	0.954 ± 0.049	0.076 ± 0.002	58.40	0.894 ± 0.052	9.89 ± 0.49	11.07
1.495	1.092 ± 0.032	0.076 ± 0.001	58.40	0.781 ± 0.025	7.51 ± 0.48	9.62
2.103	1.482 ± 0.033	0.080 ± 0.001	56.92	0.547 ± 0.014	6.08 ± 0.47	11.12

Table 7: Fitting parameters and calculated diffusion coefficients: PS-NP

$\eta/mPas$	$\tau_{ }/ms$	$(z_0/r_0)^2$	r_0/nm	$D_{NanoPCGS}/\mu m^2 s^{-1}$	$D_{DLS}/\mu m^2 s^{-1}$	$D_{DLS}/D_{NanoPCGS}$
1.075	1.456 ± 0.065	0.081 ± 0.001	56.57	0.550 ± 0.045	6.75 ± 0.27	12.28
1.495	1.754 ± 0.033	0.083 ± 0.001	55.88	0.445 ± 0.025	4.79 ± 0.23	10.76
2.103	2.343 ± 0.058	0.088 ± 0.001	54.27	0.314 ± 0.016	3.47 ± 0.13	11.04

Part V

References

- [1] M. E. Vance, T. Kuiken, E. P. Vejerano, S. P. McGinnis, M. F. Hochella, D. Rejeski, M. S. Hull, *Beilstein Journal of Nanotechnology* **2015**, *6*, 1769–1780.
- [2] P. K. Jain, X. H. Huang, I. H. El-Sayed, M. A. El-Sayed, *Accounts of Chemical Research* **2008**, *41*, 1578–1586.
- [3] P. Rivera-Gil, D. J. De Aberasturi, V. Wulf, B. Pelaz, P. Del Pino, Y. Y. Zhao, J. M. De La Fuente, I. R. De Larramendi, T. Rojo, X. J. Liang, W. J. Parak, *Accounts of Chemical Research* **2013**, *46*, 743–749.
- [4] M. Hu, J. Y. Chen, Z. Y. Li, L. Au, G. V. Hartland, X. D. Li, M. Marquez, Y. N. Xia, *Chemical Society Reviews* **2006**, *35*, 1084–1094.
- [5] A. Vogel, V. Venugopalan, *Chemical Reviews* **2003**, *103*, 577–644; Corrigendum: **2003**, *103*, 2079.
- [6] H. W. Liao, C. L. Nehl, J. H. Hafner, *Nanomedicine* **2006**, *1*, 201–208.
- [7] J. Y. Chen, D. L. Wang, J. F. Xi, L. Au, A. Siekkinen, A. Warsen, Z. Y. Li, H. Zhang, Y. N. Xia, X. D. Li, *Nano Letters* **2007**, *7*, 1318–1322.
- [8] V. Mani, B. V. Chikkaveeraiah, V. Patel, J. S. Gutkind, J. F. Rusling, *ACS Nano* **2009**, *3*, 585–594.
- [9] J. N. Anker, W. P. Hall, O. Lyandres, N. C. Shah, J. Zhao, R. P. Van Duyne, *Nature Materials* **2008**, *7*, 442–453.
- [10] L. J. Sherry, R. C. Jin, C. A. Mirkin, G. C. Schatz, R. P. Van Duyne, *Nano Letters* **2006**, *6*, 2060–2065.
- [11] C. Bohren, D. Huffman, *Absorption and Scattering of Light by Small Particles*, Wiley-Interscience, 2nd ed., **1998**.
- [12] K. M. Mayer, J. H. Hafner, *Chemical Reviews* **2011**, *111*, 3828–3857.
- [13] R. Gans, *Annalen der Physik* **1912**, *342*, 881–900.
- [14] A. Jakab, C. Rosman, Y. Khalavka, J. Becker, A. Trugler, U. Hohenester, C. Sonnichsen, *ACS Nano* **2011**, *5*, 6880–6885.

- [15] S. W. Prescott, P. Mulvaney, *Journal of Applied Physics* **2006**, *99*, 123504; Corrigendum: **2008**, *103*, 119901.
- [16] S. Link, M. B. Mohamed, M. A. El-Sayed, *Journal of Physical Chemistry B* **1999**, *103*, 3073–3077; Corrigendum: **2005**, *109*, 10531–10532.
- [17] I. Tokareva, S. Minko, J. H. Fendler, E. Hutter, *Journal of the American Chemical Society* **2004**, *126*, 15950–15951.
- [18] J. Perez-Juste, I. Pastoriza-Santos, L. M. Liz-Marzan, P. Mulvaney, *Coordination Chemistry Reviews* **2005**, *249*, 1870–1901.
- [19] G. W. Bryant, F. J. G. De Abajo, J. Aizpurua, *Nano Letters* **2008**, *8*, 631–636.
- [20] U. Hohenester, A. Trugler, *Computer Physics Communications* **2012**, *183*, 370–381.
- [21] S. Barbosa, A. Agrawal, L. Rodriguez-Lorenzo, I. Pastoriza-Santos, R. A. Alvarez-Puebla, A. Kornowski, H. Weller, L. M. Liz-Marzan, *Langmuir* **2010**, *26*, 14943–14950.
- [22] J. Becker, A. Trugler, A. Jakab, U. Hohenester, C. Sonnichsen, *Plasmonics* **2010**, *5*, 161–167.
- [23] T. Antosiewicz, M. Käll, *The Journal of Physical Chemistry C* **2016**.
- [24] G. J. Nusz, A. C. Curry, S. M. Marinakos, A. Wax, A. Chilkoti, *ACS Nano* **2009**, *3*, 795–806.
- [25] H. Siedentopf, R. Zsigmondy, *Annalen der Physik* **1903**, *10*, 1–39.
- [26] A. Wax, K. Sokolov, *Laser & Photonics Reviews* **2009**, *3*, 146–158.
- [27] J. A. Yang, H. T. Phan, S. Vaidya, C. J. Murphy, *Nano Letters* **2013**, *13*, 2295–2302.
- [28] C. Rosman, S. Pierrat, A. Henkel, M. Tarantola, D. Schneider, E. Sunnick, A. Janshoff, C. Sonnichsen, *Small* **2012**, *8*, 3683–3690.
- [29] J. Olson, S. Dominguez-Medina, A. Hoggard, L. Y. Wang, W. S. Chang, S. Link, *Chemical Society Reviews* **2015**, *44*, 40–57.
- [30] C. Rosman, J. Prasad, A. Neiser, A. Henkel, J. Edgar, C. Sonnichsen, *Nano Letters* **2013**, *13*, 3243–3247.
- [31] M. A. Beuwer, M. W. J. Prins, P. Zijlstra, *Nano Letters* **2015**, *15*, 3507–3511.
- [32] V. Lopez-Puente, S. Abalde-Cela, P. C. Angelome, R. A. Alvarez-Puebla, L. M. Liz-Marzan, *Journal of Physical Chemistry Letters* **2013**, *4*, 2715–2720.

- [33] R. Ahijado-Guzman, J. Prasad, C. Rosman, A. Henkel, L. Tome, D. Schneider, G. Rivas, C. Sonnichsen, *Nano Letters* **2014**, *14*, 5528–5532.
- [34] I. Ament, J. Prasad, A. Henkel, S. Schmachtel, C. Sonnichsen, *Nano Letters* **2012**, *12*, 1092–1095.
- [35] E. Luthgens, A. Janshoff, *Chemphyschem* **2005**, *6*, 444–448.
- [36] C. Sonnichsen, S. Geier, N. E. Hecker, G. von Plessen, J. Feldmann, H. Ditlbacher, B. Lamprecht, J. R. Krenn, F. R. Aussenegg, V. Z. H. Chan, J. P. Spatz, M. Moller, *Applied Physics Letters* **2000**, *77*, 2949–2951.
- [37] W. Stober, A. Fink, E. Bohn, *Journal of Colloid and Interface Science* **1968**, *26*, 62–69.
- [38] L. M. Liz-Marzan, M. Giersig, P. Mulvaney, *Langmuir* **1996**, *12*, 4329–4335.
- [39] I. Gorelikov, N. Matsuura, *Nano Letters* **2008**, *8*, 369–373.
- [40] Y. S. Chen, W. Frey, S. Kim, K. Homan, P. Kruizinga, K. Sokolov, S. Emelianov, *Optics Express* **2010**, *18*, 8867–8877.
- [41] E. Gergely-Fulop, D. Zambo, A. Deak, *Materials Chemistry and Physics* **2014**, *148*, 909–913.
- [42] I. I. Slowing, J. L. Vivero-Escoto, C. W. Wu, V. S. Y. Lin, *Advanced Drug Delivery Reviews* **2008**, *60*, 1278–1288.
- [43] C. Fernandez-Lopez, C. Mateo-Mateo, R. A. Alvarez-Puebla, J. Perez-Juste, I. Pastoriza-Santos, L. M. Liz-Marzan, *Langmuir* **2009**, *25*, 13894–13899.
- [44] M. Son, J. Lee, D. J. Jang, *Journal of Molecular Catalysis a-Chemical* **2014**, *385*, 38–45.
- [45] D. Bruhwiler, *Nanoscale* **2010**, *2*, 887–892.
- [46] W. C. Wu, J. B. Tracy, *Chemistry of Materials* **2015**, *27*, 2888–2894.
- [47] N. S. Abadeer, M. R. Brennan, W. L. Wilson, C. J. Murphy, *ACS Nano* **2014**, *8*, 8392–8406.
- [48] W. S. Chang, J. W. Ha, L. S. Slaughter, S. Link, *Proceedings of the National Academy of Sciences of the United States of America* **2010**, *107*, 2781–2786.
- [49] D. Y. Zhao, J. L. Feng, Q. S. Huo, N. Melosh, G. H. Fredrickson, B. F. Chmelka, G. D. Stucky, *Science* **1998**, *279*, 548–552.
- [50] M. N. Sanz-Ortiz, K. Sentosun, S. Bals, L. M. Liz-Marzan, *Acs Nano* **2015**, *9*, 10489–10497.
- [51] J. Heidrich, V. Wulf, R. Hennig, M. Saur, J. Markl, C. Sonnichsen, D. Schneider, *Journal of Biological Chemistry* **2016**.

- [52] R. Hennig, J. Heidrich, M. Saur, L. Schmuser, S. J. Roeters, N. Hellmann, S. Woutersen, M. Bonn, T. Weidner, J. Markl, D. Schneider, *Nature Communications* **2015**, *6*, year.
- [53] U. C. Vothknecht, S. Otters, R. Hennig, D. Schneider, *Journal of Experimental Botany* **2012**, *63*, 1699–1712.
- [54] E. Fuhrmann, J. B. Bultema, U. Kahmann, E. Rupprecht, E. J. Boekema, D. Schneider, *Molecular Biology of the Cell* **2009**, *20*, 4620–4628.
- [55] D. Kroll, K. Meierhoff, N. Bechtold, M. Kinoshita, S. Westphal, U. C. Vothknecht, J. Soll, P. Westhoff, *Proceedings of the National Academy of Sciences of the United States of America* **2001**, *98*, 4238–4242.
- [56] C. L. Baciú, J. Becker, A. Janshoff, C. Sonnichsen, *Nano Letters* **2008**, *8*, 1724–1728.
- [57] C. Lambertz, A. Martos, A. Henkel, A. Neiser, T. Kliesch, A. Janshoff, P. Schwille, C. Sonnichsen, *Nano Letters* **2016**.
- [58] C. J. Orendorff, T. M. Alam, D. Y. Sasaki, B. C. Bunker, J. A. Voigt, *ACS Nano* **2009**, *3*, 971–983.
- [59] G. Raschke, S. Kowarik, T. Franzl, C. Sonnichsen, T. A. Klar, J. Feldmann, A. Nichtl, K. Kurzinger, *Nano Letters* **2003**, *3*, 935–938.
- [60] Z. Adamczyk, P. Weroniski, *Journal of Chemical Physics* **1996**, *105*, 5562–5573.
- [61] D. Magde, W. W. Webb, E. Elson, *Physical Review Letters* **1972**, *29*, 705–708.
- [62] K. L. Wang, X. Qiu, C. Q. Dong, J. C. Ren, *Chembiochem* **2007**, *8*, 1126–1129.
- [63] C. L. Kuyper, B. S. Fujimoto, Y. Zhao, P. G. Schiro, D. T. Chiu, *Journal of Physical Chemistry B* **2006**, *110*, 24433–24441.
- [64] H. Liu, C. Q. Dong, X. Y. Huang, J. C. Ren, *Analytical Chemistry* **2012**, *84*, 3561–3567.
- [65] H. Liu, C. Q. Dong, J. C. Ren, *Journal of the American Chemical Society* **2014**, *136*, 2775–2785.
- [66] T. E. Starr, N. L. Thompson, *Biophysical Journal* **2001**, *80*, 1575–1584.
- [67] P. Schwille, E. Haustein, *Fluorescence Correlation Spectroscopy: An Introduction to its Concepts and Applications*, Biophysics Textbook online, **2002**.
- [68] B. Trankle, D. Ruh, A. Rohrbach, *Soft Matter* **2016**, *12*, 2729–2736.
- [69] J. Happel, H. Brenner, *Low Reynolds Number Hydrodynamics*, Vol. 40, Kluwer Academic Publishers, **1991**.

[70] X. C. Ye, C. Zheng, J. Chen, Y. Z. Gao, C. B. Murray, *Nano Letters* **2013**, *13*, 765–771.

[71] J. Turkevich, P. C. Stevenson, J. Hillier, *Discussions of the Faraday Society* **1951**, 55–75.

Part VI

Acknowledgment

personal data removed

Part VII

Curriculum Vitae

personal data removed